Computational Geosciences (2023) 27:829–851
https://doi.org/10.1007/s10596-023-10234-1

ORIGINAL PAPER

An extended peridynamic bond-based constitutive model for simulation of crack propagation in rock-like materials

Gang Sun[1] · Junxiang Wang[1] · Haiyue Yu[1] · Lianjun Guo[1]

Received: 10 February 2023 / Accepted: 14 June 2023 / Published online: 26 July 2023

Abstract
The stress of rock-like materials first increases and then decreases with an increase in the strain, and finally become damaged under tensile or compressive loads. It is not suitable to use the traditional bond-based peridynamics model to simulate the crack propagation of rock-like materials. Based on the bond-based peridynamics theory, a constitutive model has here been proposed that can reflect the characteristic of the stress with an increase in strain (i.e., that the stress of the rock-like materials first increases and then decreases, and finally fails). This makes up for the weakness with the traditional bond-based peridynamics theory, which fails to reflect the stress-strain change in rock-like materials. The strain energy density of the proposed constitutive model of rock-like materials has been derived and compared against the classical elasticity theory to obtain the model constants with respect to the elasticity moduli for plane stress conditions. Based on the here proposed constitutive model for rock-like materials, a numerical solution program for rock-like materials has been written using the Fortran language. For different loading conditions, the crack propagation process for an intact specimen has been simulated and compared with experimental results. This was also the situation for a specimen with a pre-existing flaw, a single non-straight flaw, and with three pre-existing flaws for plane stress conditions. The numerical simulation results were in good agreement with the corresponding experimental results. By using this proposed constitutive model, it was possible to simulate and predict the mechanical properties of rock-like materials, and the process of crack initiation, propagation, and coalescence under different loading conditions. The results from the present study can thus provide a reference for practical engineering.

Keywords Constitutive model · Peridynamic · Crack propagation · Rock-like materials · Crack coalescence

1 Introduction

Rock is a type of natural material that contains a number of microcracks with different directions. Under various loading conditions, these cracks can initiate, propagate, interact, and coalesce, which eventually leads to a failure of rock bulk. Therefore, the investigation of the mechanism of crack initiation, propagation, and coalescence is of the largest importance for geotechnical engineering construction.

To explore the mechanisms of rock crack initiation, propagation, and interaction, some researchers have studied the crack morphology by performing experiments on single flaw rock specimens under uniaxial compression [1–6]. Due to the possibility of two or more flaws in actual engineering, numerous laboratory experiments have been performed in studying the crack coalescence modes of rock-like materials under the condition of double, or multiple, flaws [2, 7–11]. The results from these studies showed that the crack propagation mode depended on the number and geometric arrangement of the flaws. Wing cracks and secondary cracks are the main forms of crack propagation. As is the situation with tension cracks, the initiating position of the wing crack is influenced by the flaw inclination angle. With an increasing flaw inclination angle, the wing crack initiation position moves to the tip of the pre-existing crack [2, 6]. Furthermore, secondary cracks are usually considered as shear cracks, and appear later. These experiments are of a major importance for an understanding of the crack propagation processes and coalescence mechanism. However, there are still some limitations in these experiments; (1) Due to the instantaneity of the crack propagation, it is difficult to obtain any relevant fracture parameters from the experiments. (2) The experimental investigations of the crack propagation mechanism are time consuming, costly,

✉ Junxiang Wang
w.j.xgood@163.com

[1] School of Architecture and Civil Engineering, Shenyang University of Technology, Shenyang 110870, China

and poorly reproducible. At present, numerical simulations have become an important method for studying crack propagation in rock-like materials.

These theoretical methods are based on the theory of continuum media mechanics and include the finite element method (FEM) [12, 13], finite difference method (FDM) [14, 15], boundary element method (BEM) [16] and extended finite element method (XFEM) [17–19], which have earlier been used to simulate the process of crack initiation, propagation, and coalescence. However, there are certain inherent flaws in these numerical methods. For instance, the spatial partial differential equation is not defined at the discontinuity for the situation with an object discontinuity. Furthermore, there will be a singularity problem at the crack tip when using numerical solutions. This can be explained by the fact that the equations of motion of the FEM, FDM, and BEM have been represented by spatial partial differential equations. The usage of XFEM, it is possible to simulate crack propagation by defining enrichment functions. However, for the strengthening of a discontinuous displacement field, it is still necessary to introduce external criteria. And it is difficult to define enrichment functions in the process of dealing with some complex fracture problems (such as crack branching and coalescence).

The numerical manifold method (NMM) [20–22], discontinuous deformation analysis (DDA) [23, 24], and discrete element method (DEM) [25, 26] are several common numerical methods that have a made large progress in solving fracture problems. They are based on the mechanics of discontinuous media. The crack tip is constrained by an element boundary when NMM is used for simulating the crack propagation, which will influence the accuracy of the calculations. On the other hand, the crack propagation path when using DDA depends on the size of discrete blocks. It is, therefore, difficult to simulate the whole process from continuity to cracking of objects [27]. Due to the lack of theoretical accuracy of DEM, the calculation of the continuum deviates greatly from the reality.

For the past few years, an emerging meshless method has been proposed by Silling [28]. It is based on a nonlocal action, peridynamics (PD), which reconstructs the equations of motion of solid mechanics in an integral form. It can also solve the problem with traditional methods, which are not defined for solutions at discontinuities. Furthermore, it can simulate the process of spontaneous crack propagation without externally defined criteria, which is widely used in the study of fracture behavior of materials [29–31]. The PD is classified into four types: bond-based, ordinary-state-based, non-ordinary-state-based [32, 33] and the bond-associated PD models [34–38]. The bond-associated PD models [34–37] which are able to incorporate classical constitutive models on the level (rather than on the point level) and has superior stability over the non-ordinary state-based PD. It has been shown that the bond-associative PD technique is effective for capturing complicated failure processes, e.g. ductile failures [38], failures in concrete materials [39], and concrete spalling [40, 41]. The other three methods have also been used to probe the process of crack propagation and the mechanisms of action of rock-like materials, such as the splitting damage of Brazilian discs under impact loading [42–44], cracking mechanism of liquid carbon dioxide [45], crack propagation behavior of flaws under compressive loading [46–49], calculation of fracture toughness [50, 51], and hydraulic fracturing [52]. Among these ones, the micro-elastic brittle model of bond-based peridynamics is the most extensively used one. It has been considered that the particles are connected by bonds, and the interaction between the binding particles can be expressed by a pairwise force function. Also, the functions varies linearly with the bond stretch. When the bond stretch exceeds a critical stretch, the bond between the two particles breaks and the intrapair interaction disappears. This is inconsistent with the characteristics of rock-like material, namely that the stress will first increase, then reduce, and a damage will finally occur, with an increase in strain. Accordingly, researchers plumb fracture behaviors of rock-like materials by improving the pairwise force function [53–55]. To mention but a few, Wang et al. [53] established a constitutive model of concrete materials in studying the effect of pulse forms, pulse load action time, and model geometry of spallation. Zhou et al. [54] proposed a micro-elastoplastic constitutive model to investigate the crack propagation process of single flaw under uniaxial compression. Zhou et al. [55] proposed an improved peridynamics model to study the influence of preexisting flaws with different lengths and inclination angles on the crack propagation length of wing cracks. On the basis of these observations, it is clear that the traditional micro-elastic brittle constitutive model fails to reflect the characteristics of the rock-like materials strain hardening, with a following strain softening. Whereas the improved peridynamics model mostly describes the nonlinear deformation stage of the bond in the form of exponential or logarithmic functions, it is difficult to get a general analytical solution [56].

We have proposed a new constitutive model, that is based on the traditional micro-elastic brittle model, to describe the linear and nonlinear mechanical behavior of rock-like materials. It considers not only the linear elastic deformation phase of the bond, but also the nonlinear deformation phase of the bond, which is described by a quadratic function. The strain energy density of the proposed constitutive model of rock-like materials has been derived and compared against the classical elasticity theory to obtain the model constants with respect to the elasticity moduli for plane stress conditions. Under different loading conditions, the processes of crack initiation, propagation, and coalescence of intact specimens, as well as a single straight fissure, and three

pre-existing flaws specimens, have been simulated using the proposed constitutive model. In comparison with available experimental results [8, 57], the proposed constitutive model shows the effectiveness in simulating crack propagation and coalescence patterns under different loading conditions.

2 Constitutive model of rock-like materials based on the peridynamic

2.1 Peridynamic theory

As a new meshless method, peridynamic theory reconstructs the equation of motion of solid mechanics with the spatial integral of displacement, avoiding the problem that the traditional method undefined at the discontinuity. As shown in Fig. 1, in peridynamics theory, the body is discretized into a large number of material points with volume V_x and mass density ρ in the spatial domain. Material point $\mathbf{x}$ only interacts with another material points $x^{'}$ in its horizon $H=\{x^{'}\in R, \|x^{'}-x\|<\delta\}$, the interaction is described by the pairwise force function $\mathbf{f}$. According to Newton's second law, the equation of motion of a material point at time t can be expressed as:

$$\rho(x)\ddot{u}(x,t)=\int_H f\left(x',x,u\left(x',t\right),u(x,t),t\right)dV_x'+b(x,t) \quad (1)$$

where $x^{'}$ is the material point in the $\mathbf{x}$ horizon, $u(x,t)$ denotes the displacement of material point $\mathbf{x}$, $\rho(x)$ and $\ddot{u}(x,t)$ are the mass density and acceleration of material point $\mathbf{x}$, dV_x' represents infinitesimal volume of material point $x^{'}$, $H=\{x^{'}\in R, \|x^{'}-x\|<\delta\}$ is a spherical subregion of material point $\mathbf{x}$ including material point $x^{'}$, $\mathbf{f}$ denotes the pairwise force function related to the properties of the material, and

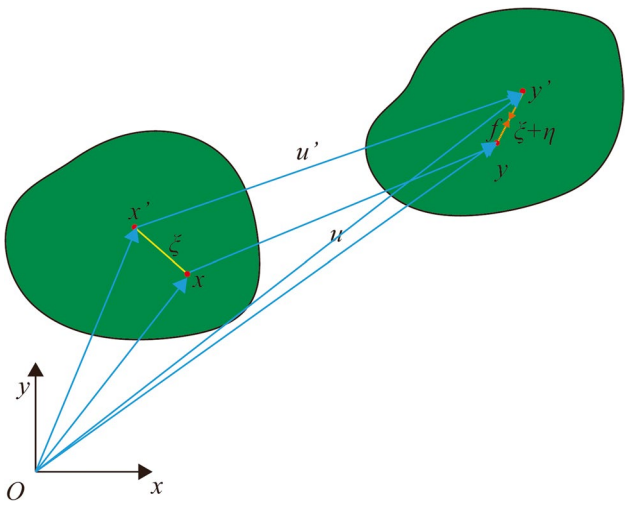

Fig. 1 An illustration of Kinematics of peridynamics material points

$b(x,t)$ is the body force density. It should be noted that Eq. (1) only applies to bond-based peridynamics models.

2.2 Constitutive model of elastic-brittle materials

The prototype micro-elastic brittle (PMB) model of isotropic materials proposed by Silling and Askari [58] is one of the most roundly applied constitutive models, of which pairwise force function can be given as:

$$f(\eta,\xi)=\frac{\partial\omega(\eta,\xi)}{\partial\eta}\forall\xi,\eta \quad (2)$$

where $\eta=u^{'}-u$ and $\xi=x^{'}-x$ are relative displacement vectors and relative position vectors, $\omega(\eta,\xi)$ is micro-potential function, which is a scalar-valued function characterizing the strength of the interaction between material points, the micro-potential represents energy of a bond, the strain energy density of a material point is found form

$$W=\frac{1}{2}\int_{H_x}\omega(\xi,\eta)dV_x' \quad (3)$$

where 1/2 indicates that the energy at the material point is half of the energy of the interacting bond.

In the bond-based peridynamics, the deformation of a material point pair is defined as the bond stretch. The formation of cracks is related to the fracture of bonds, the bond stretch is stated as

$$s=\frac{(|\xi+\eta|-|\xi|)}{|\xi|} \quad (4)$$

where $|\xi|$ denotes initial length of bond, and $|\xi+\eta|$ represents length of deformed bond.

The relation between pairwise force and bond stretch is illustrated in Fig. 2. In the constitutive model of PMB materials, the scalar-valued function of the pairwise force has a linear relationship with the bond stretch and can be written as $f=cs$. Assuming that the homogeneous body expands isotropic, the relative displacement can be expressed as $\eta=s\xi$. The micro-potential function is given as

$$\omega(\eta,\xi)=\int_0^{s\xi}\boldsymbol{csd\eta}=\int_0^{s\xi}c\frac{\eta}{\xi}=\frac{cs^2\xi}{2} \quad (5)$$

where, c represents the micro-modulus, which is similar to the elastic modulus in the continuum mechanics theory and represents the deformation characteristics of material. It can be obtained by equating the strain energy density of the continuum mechanics with the peridynamic strain energy density when uniform deformation occurs. For the plane stress problem, the micro-modulus c is given by

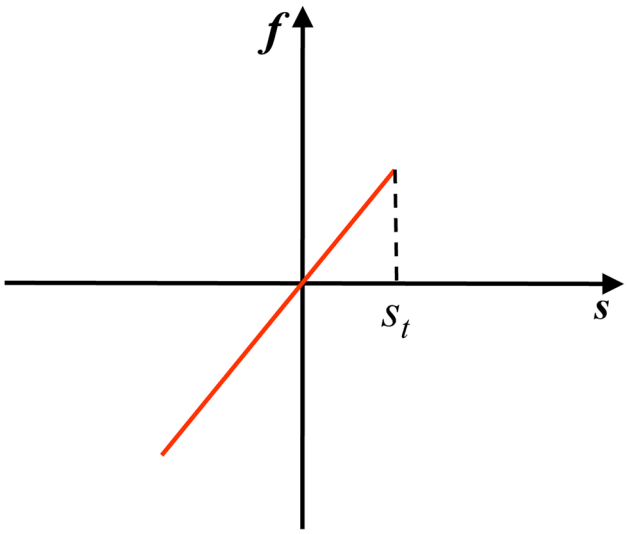

Fig. 2 The pairwise force function of PMB materials

$$c = \frac{6E}{\pi h \delta^3 (1-\nu)} \tag{6}$$

where, E and h are the Young's modulus and the thickness; δ is the size of horizon.

The pairwise force function is connected with the relative position and relative displacement of material points $\boldsymbol{x}$ and x', and the direction of the pairwise force is consistent with the deformation direction of bond. When the bond stretch s between two corresponding material points exceeds the critical stretch s_0, the bond breaks, and there is no pairwise force between two points. It is noted that the bond breaks irreversibly, once a bond is broken, it is broken forever even if we unload the material. Then the pairwise force **f** can be expressed as:

$$f(\eta, \xi) = f(\eta, \xi)\frac{\xi+\eta}{|\xi+\eta|} = \begin{cases} cs\frac{\xi+\eta}{|\xi+\eta|} s \le s_0 \\ 0 \quad \textbf{\textit{others}} \end{cases} \tag{7}$$

One of the advantages of peridynamic is that it can judge the failure of materials without introducing other additional criteria. In the peridynamic theory, the local damage of a material point is expressed by the ratio of the disappeared interaction in its horizon to the original total interaction, which is capable of calculating as follows:

$$\varphi(x,t) = 1 - \frac{\int_{H_x} \mu(x,t,\xi) dV_\xi}{\int_{H_x} dV_\xi} \tag{8}$$

where, $\mu(x,t,\xi)$ is a scalar-valued function representing the bond status and take the value of 0 for broken bonds and 1 for intact bonds; $0 \le \varphi \le 1$, $\varphi = 0$ represents that the material point is not damaged, and $\varphi = 1$ means that the material point is completely damaged.

2.3 Constitutive model of rock-like materials

The PMB model mentioned above considers that the pairwise force changes linearly with the bond stretch, which is similar to the linear elastic material in traditional elasticity. When the stress reaches the peak value, the material suddenly fails. Obviously, this model is not suitable for the failure of rock-like materials. Both compressive and tensile strength of rock-like materials have obvious characteristics of strain hardening subsequent strain softening, that is, the stress first increases, then reduces and finally damages along with strain. In order to accurately simulate the crack propagation process of rock-like materials, based on previous studies [53, 56] and combining the characteristics of tensile and compressive curves of rock-like materials, this paper proposes a constitutive model which can reflect the linear and nonlinear mechanical behavior of rock-like materials. The pairwise force function of the constitutive model is shown in Fig. 3.

In the pairwise force function, the bond stretch s is in the range of $s_{1c} \le s \le s_{1t}$, the bond is in the state of linear elastic deformation, the relationship between pairwise force and stretch is linear, and the bond has no damage. The bond stretch s is in the range of $s_{1t} < s < s_t$ or $s_{1c} < s < s_c$, the bond is in the nonlinear deformation stage. The nonlinear deformation of bond falls into two stages, nonlinear strengthening deformation and nonlinear softening deformation stage. While $s_{1t} < s < s_{2t}$ or $s_{1c} < s < s_{2c}$, the bond is in the nonlinear strengthening deformation stage, then its damage occurs leading to the appearance of microcracks, the pairwise force increases nonlinearly with bond stretch. When $s_{2t} < s < s_t$ or $s_{2c} < s < s_c$, the bond is in the nonlinear

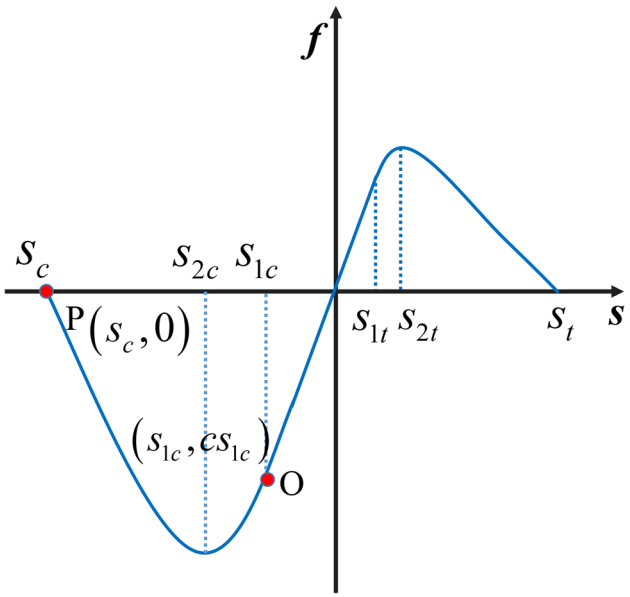

Fig. 3 The pairwise force function of rock-like materials

softening stage and the pairwise force decreases nonlinearly with bond stretch. When $s > s_t$ or $s < s_c$, the bond damage is 1, the bond is allowed to break irreversibly, and there is no interaction between two material points.

Assuming that the scalar-valued function of the pairwise force in the nonlinear deformation stage of the bond is

$$f = A's^2 + B's + C' \tag{9}$$

As can be seen from Fig. 3, for the compression stage of the bond, the scalar-valued function of the pairwise force f passes through the point O (s_{1c},cs_{1c}), P (s_c,0). Substituting the coordinates of O and P into the Eq. (9), it leads to Eq. (10)

$$\begin{cases} A's_{1c}^2 + B's_{1c} + C' = cs_{1c} \\ A's_c^2 + B's_c + C' = 0 \end{cases} \tag{10}$$

Since the scalar-valued function f of pairwise force is a quadratic function.

$$-\frac{B'}{2A'} = s_{2c} \tag{11}$$

Substituting Eq. (11) into Eq. (10), Eq. 12 is obtained as follows:

$$\begin{cases} A' = \frac{cs_{1c}}{(s_{1c}-s_c)(s_{1c}+s_c-2s_{2c})} \\ B' = \frac{-2cs_{1c}s_{2c}}{(s_{1c}-s_c)(s_{1c}+s_c-2s_{2c})} \\ C' = \frac{cs_{1c}s_c(2s_{2c}-s_c)}{(s_{1c}-s_c)(s_{1c}+s_c-2s_{2c})} \end{cases} \tag{12}$$

where s_c denotes the fracture stretch of compression, s_{2c} is the critical stretch of compression, s_{1c} is the compression elastic stretch.

Similar to Eq. (12) we get

$$\begin{cases} D' = \frac{cs_{1t}}{(s_{1t}-s_t)(s_{1t}+s_t-2s_{2t})} \\ E' = \frac{-2cs_{1t}s_{2t}}{(s_{1t}-s_t)(s_{1t}+s_t-2s_{2t})} \\ F' = \frac{cs_{1t}s_t(2s_{2t}-s_t)}{(s_{1t}-s_t)(s_{1t}+s_t-2s_{2t})} \end{cases} \tag{13}$$

where s_t represents the fracture stretch of tensile, s_{2t} is the critical stretch of tensile, s_{1t} represents tensile elastic stretch.

In the present model, the critical strength of the bond (s_{2t},s_{2c}) of rock-like materials is related to the fracture strength [59, 60] and can be expressed as:

$$\begin{cases} s_{2t} = \frac{f_t}{E} \\ s_{2c} = -\frac{f_c}{E} \end{cases} \tag{14}$$

where, f_t and f_c are the uniaxial tensile and uniaxial compressive strengths of the materials, respectively; E is the Young's modulus.

The elastic stretch (s_{1t},s_{1c}) and fracture stretch (s_t,s_c) of the bond under tension and compression of rock-like materials can be given as follows:

$$\begin{cases} s_{1t} = \gamma_t s_{2t} \quad s_t = \beta_t s_{2t} \\ s_{1c} = \gamma_c s_{2c} \quad s_c = \beta_c s_{2c} \end{cases} \tag{15}$$

where, γ_t and γ_c are the microscopic parameters of the rock-like materials constitutive model, which can be obtained from the geometric relationship between the bond stretch and bond force [61, 62]. β_t and β_c are the microscopic parameters of the rock-like material constitutive model. β_t can be adjusted to match the fracture energy of the rock-like materials, and β_c can be adjusted to represent the uniaxial compressive energy absorption capacity of the rock-like materials. Similar methods can be found in literature [49, 59–62] to determine fracture stretch of the bond.

Considering local damage of the bond, the pairwise force function of rock-like materials is expressed as

$$f(\eta, \xi) = cs(1 - \alpha(s))\frac{\eta + \xi}{|\eta + \xi|} \tag{16}$$

Where $\alpha(s)$ is a scalar-valued function representing progressive damage of the bond, which is given as follows:

$$\alpha(s) = \begin{cases} 1 - \left(\frac{A's}{c} + \frac{B'}{c} + \frac{C'}{cs}\right) & s_c \le s < s_{1c} \\ 0 & s_{1c} \le s \le s_{1t} \\ 1 - \left(\frac{D's}{c} + \frac{E'}{c} + \frac{F'}{cs}\right) & s_{1t} < s \le s_t \\ 1 & others \end{cases} \tag{17}$$

Let $\begin{pmatrix} A' & B' & C' & D' & E' & F' \end{pmatrix} = c\begin{pmatrix} A_1 & B_1 & C_1 & D_1 & E_1 & F_1 \end{pmatrix}$, $\alpha(s)$ can be expressed as

$$\alpha(s) = \begin{cases} 1 - \left(A_1 s + B_1 + \frac{C_1}{s}\right) & s_c \le s < s_{1c} \\ 0 & s_{1c} \le s \le s_{1t} \\ 1 - \left(D_1 s + E_1 + \frac{F_1}{s}\right) & s_{1t} < s \le s_t \\ 1 & others \end{cases} \tag{18}$$

The range of $\alpha(s)$ is [0,1], when the value of $\alpha(s)$ is 0, the bond not damaged. When the value of $\alpha(s)$ is 1, the bond is broken, and there is no interaction between two material points.

Then, the strain energy density and micro-modulus of rock materials are deduced. The premise of derivation is consistent with the PMB model, the scalar-valued function of the pairwise force for rock-like materials is

$$f(\boldsymbol{\eta}, \boldsymbol{\xi}) = \begin{cases} A's^2 + B's + C' & s_c \le s < s_{1c} \\ cs & s_{1c} \le s \le s_{1t} \\ D's^2 + E's + F' & s_{1t} < s \le s_t \\ 0 & \text{others} \end{cases} \tag{19}$$

The micro-potential can be solved by the method of PMB material model for the linear elastic deformation stage. For the

nonlinear deformation stage, the micro-potential includes the energy in the linear elastic deformation stage and the energy in the nonlinear deformation stage, and the micro-potential function is stated as

$$\omega = \begin{cases} \int_0^{s_{1c}\xi} f(\boldsymbol{\eta},\boldsymbol{\xi})d\eta + \int_{s_{1c}\xi}^{s\xi} f(\boldsymbol{\eta},\boldsymbol{\xi})d\eta & s_c \le s < s_{1c} \\ \int_0^{s\xi} f(\boldsymbol{\eta},\boldsymbol{\xi})d\eta & s_{1c} \le s \le s_{1t} \\ \int_0^{s_{1t}\xi} f(\boldsymbol{\eta},\boldsymbol{\xi})d\eta + \int_{s_{1t}\xi}^{s\xi} f(\boldsymbol{\eta},\boldsymbol{\xi})d\eta & s_{1t} < s \le s_t \end{cases} \tag{20}$$

Substituting the scalar-valued function of the pairwise force in Eq. (19) into Eq. (20), the micro-potential function is expressed as

$$\omega = \begin{cases} \int_0^{s_{1c}\xi} csd\eta + \int_{s_{1c}\xi}^{s\xi} \left(A's^2 + B's + C'\right)d\eta & s_c \le s < s_{1c} \\ \int_{\xi}^{s\xi} csd\eta & s_{1c} \le s \le s_{1t} \\ \int_0^{s_{1t}\xi} csd\eta + \int_{s_{1t}\xi}^{s\xi} \left(D's^2 + E's + F'\right)d\eta & s_{1t} < s \le s_t \end{cases} \tag{21}$$

The derivation premise is isotropic expansion, we have $\eta = s\xi$, the micro-potential function can further be written as

$$\omega = \begin{cases} \int_0^{s_{1c}\xi} c\frac{\eta}{\xi}d\eta + \int_{s_{1c}\xi}^{s\xi} \left(A'\left(\frac{\eta}{\xi}\right)^2 + B'\frac{\eta}{\xi} + C'\right)d\eta & s_c \le s < s_{1c} \\ \int_{\xi}^{s\xi} c\frac{\eta}{\xi}d\eta & s_{1c} \le s \le s_{1t} \\ \int_0^{s_{1t}\xi} c\frac{\eta}{\xi}d\eta + \int_{s_{1t}\xi}^{s\xi} \left(D'\left(\frac{\eta}{\xi}\right)^2 + E'\frac{\eta}{\xi} + F'\right)d\eta & s_{1t} < s \le s_t \end{cases} \tag{22}$$

Integrating to formula (22), the micro-potential function of rock-like materials can be written as

$$\omega = \begin{cases} \frac{cs_{1c}^2\xi}{2} + \frac{A'\xi\left(s^3 - s_{1c}^3\right)}{3} + \frac{B'\xi\left(s^2 - s_{1c}^2\right)}{2} + C'\xi\left(s - s_{1c}\right) & s_c \le s < s_{1c} \\ \frac{cs^2\xi}{2} & s_{1c} \le s \le s_{1t} \\ \frac{cs_{1t}^2\xi}{2} + \frac{D'\xi\left(s^3 - s_{1t}^3\right)}{3} + \frac{E'\xi\left(s^2 - s_{1t}^2\right)}{2} + F'\xi\left(s - s_{1t}\right) & s_{1t} < s \le s_t \end{cases} \tag{23}$$

Substituting the micro-potential function (23) into Eq. (3), the strain energy density of rock-like materials is expressed as

$$W = \begin{cases} \frac{1}{2}\int_{V_j}\left(\frac{cs_{1c}^2\xi}{2} + \frac{A'\xi\left(s^3 - s_{1c}^3\right)}{3} + \frac{B'\xi\left(s^2 - s_{1c}^2\right)}{2} + C'\xi\left(s - s_{1c}\right)\right)dV_j & s_c \le s < s_{1c} \\ \frac{1}{2}\int_{V_j}\frac{cs^2\xi}{2}dV_j & s_{1c} \le s \le s_{1t} \\ \frac{1}{2}\int_{V_j}\left(\frac{cs_{1t}^2\xi}{2} + \frac{D'\xi\left(s^3 - s_{1t}^3\right)}{3} + \frac{E'\xi\left(s^2 - s_{1t}^2\right)}{2} + F'\xi\left(s - s_{1t}\right)\right)dV_j & s_{1t} < s \le s_t \end{cases} \tag{24}$$

The strain energy density of a material point can be obtained by integrating Eq. 24

$$W = \begin{cases} \frac{\pi h s_{1c}^2 c\delta^3}{6} + \frac{A'\pi h\delta^3\left(s^3 - s_{1c}^3\right)}{9} + \frac{B'\pi h\delta^3\left(s^2 - s_{1c}^2\right)}{6} + \frac{C'\pi h\delta^3\left(s - s_{1c}\right)}{3} & s_c \le s < s_{1c} \\ \frac{\pi h c s^2\delta^3}{6} & s_{1c} \le s \le s_{1t} \\ \frac{\pi h s_{1t}^2 c\delta^3}{6} + \frac{D'\pi h\delta^3\left(s^3 - s_{1t}^3\right)}{9} + \frac{E'\pi h\delta^3\left(s^2 - s_{1t}^2\right)}{6} + \frac{F'\pi h\delta^3\left(s - s_{1t}\right)}{3} & s_{1t} < s \le s_t \end{cases} \tag{25}$$

In 2D plane stress problems, strain energy density in traditional continuum mechanics is $U_{EL} = \frac{Es^2}{1-\nu}$. The micro-modulus c can be obtained by the strain energy density at the elastic stage of the peridynamic being equal to the strain energy density of the continuum mechanics.

$$c = \frac{6E}{(1-\nu)\pi h\delta^3} \tag{26}$$

where, E and h are the Young's modulus and the thickness; δ is the size of horizon.

2.4 Numerical solution method

In order to solve the equation of motion of peridynamic, the model is discretized uniformly. The position of the material point is determined by the center point of the square grid, so that the spatial integral equation can be converted into a finite sum solution. The equation of motion in Eq. (1) can be expressed as:

$$\rho(x)\ddot{u}_x^n = \sum_H^k f\left(\left(x'\right)^n - x^n, x' - x\right)V_{x'} + b_x^n \tag{27}$$

where, n represents the number of time steps, $\ddot{u}_x^n$ is the acceleration of the material point $\mathbf{x}$ when the time step is n, k represents the total number of material points x' in its horizon, and $V_{x'}$ represents the volume of the material point x'. If the material point is at the edge of horizon, the volume is reduced and then needs to be corrected. The corrected volume can be calculated by Eq. (28) [32].

$$V_{x'} = \begin{cases} V_{x'} & |\,\xi\,| \le (\delta - r) \\ \left(\frac{\delta + r - |\xi|}{2r}\right)V_{x'} & (\delta - r) < |\,\xi\,| \le \delta \\ 0 & |\,\xi\,| > \delta \end{cases} \tag{28}$$

Where $r = \Delta x/2$, Δx represents the side length of the square grid.

Surface effects are a disadvantage of bond-based peridynamics models owing to the fact that the horizons of material points near the domain boundaries are incomplete. In the proposed model, the authors employ the method using correction of the strain energy density [32] to reduce surface effects.

Although peridynamic is a dynamic method, quasi-static problems can be solved by dynamic relaxation method, that is, artificially adding damping to the system [63]. For purpose of selecting the appropriate damping coefficient and speeding up the convergence, the adaptive dynamic relaxation (ADR) method is employed to determine the damping coefficient of each step [63].

According to the ADR method, the virtual inertia and local damping are introduced into all material points in the system, and the equation of PD for solving static problems is obtained:

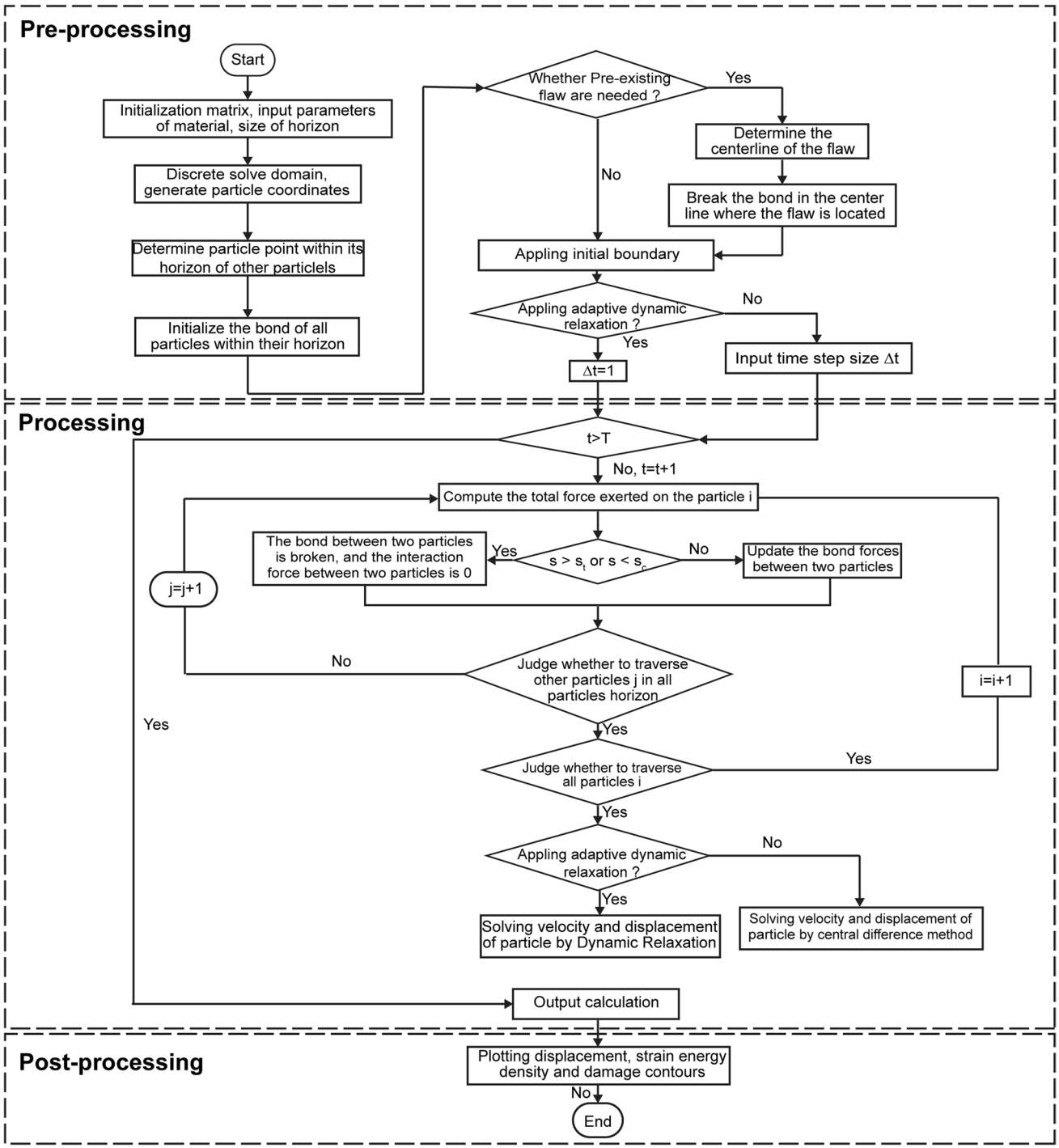

Fig. 4 The flow chart for the based-bond peridynamic program

$$\Lambda\ddot{\mathrm{u}} + c\Lambda\dot{\mathrm{u}} + \mathrm{L} = \mathrm{b} \tag{29}$$

where, Λ is the virtual diagonal density matrix; c is the damping coefficient; L is the body force density of the interaction between the material point, $\mathrm{L} = \sum_H^k \mathrm{f}(\eta^n, \xi)V_{x'}$; b is the body force density of the external force.

The method using central difference is employed to calculate the velocity and displacement at different time steps:

$$\begin{aligned} \dot{\boldsymbol{u}}^{1/2} &= \frac{\Delta t \boldsymbol{\Lambda}^{-1}\left(\boldsymbol{b}^0 - \boldsymbol{L}^0\right)}{2} \quad (n=0) \\ \dot{\boldsymbol{u}}^{n+1/2} &= \frac{(2-c^n\Delta t)}{(2+c^n\Delta t)}\dot{\boldsymbol{u}}^{n-1/2} + \frac{2\Delta t \boldsymbol{\Lambda}^{-1}\left(\boldsymbol{b}^n - \boldsymbol{L}^n\right)}{(2+c^n\Delta t)} \\ \boldsymbol{u}^{n+1} &= \boldsymbol{u}^n + \Delta t\dot{\boldsymbol{u}}^{n+1/2} \end{aligned} \tag{30}$$

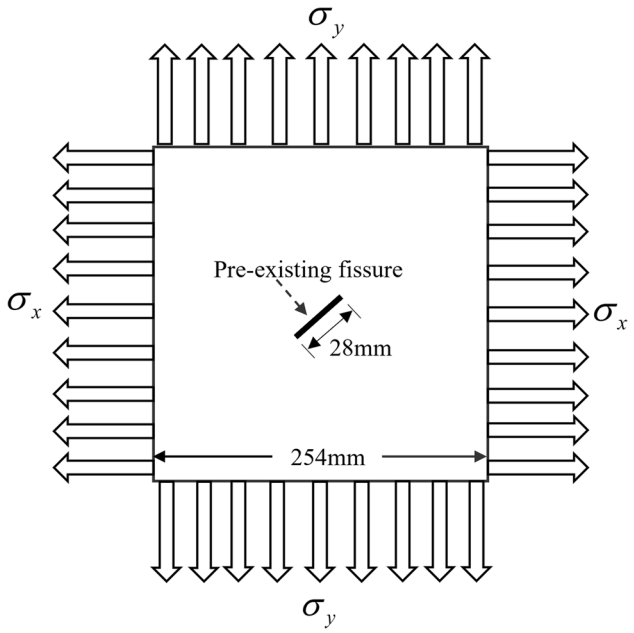

Fig. 5 Numerical model diagram

where, Δt is the time step size.

According to Eq. (30), once the density matrix Λ, damping coefficient c and time step size Δt are determined, the speed and displacement of steps at different times can be obtained.

The study of reference [64] shows that these three values do not affect the final result of the steady-state solution. Appropriate parameters should be selected based on the principle of ensuring the minimum time step convergence of the algorithm. In dynamic relaxation, a time step size of 1 is commonly used [32].

The virtual diagonal density matrix Λ is determined by Greschgorin's theorem [63]:

$$\lambda_{ii} \geq \frac{\Delta t^2}{4} \sum_{j=1}^{n} \left| \mathrm{K}_{ij} \right| \tag{31}$$

where, λ_{ii} is the diagonal element of the virtual diagonal density matrix Λ; K_{ij} is a stiffness matrix, which is expressed by the partial derivative of the interaction force between the material points with respect to the relative displacement vector:

$$\sum_{j=1}^{n} \left| \mathrm{K}_{ij} \right| = \sum_{j=1} \left| \frac{\partial f(\xi, \eta) V_j}{\partial \eta} \right| \tag{32}$$

For the selection of the damping coefficient c, the effective damping at each time step can be calculated by formula (33).

$$c^n = 2\sqrt{\left[(\mathrm{u}^n)^{\mathrm{T}1} \mathrm{K}^n \mathrm{u}^n\right] / \left[(\mathrm{u}^n)^{\mathrm{T}} \mathrm{u}^n\right]} \tag{33}$$

where, ${}^1\mathrm{K}^n$ represents the diagonal "local" stiffness matrix, ${}^1K_{ii}^n = -\left(L_i^n/\lambda_{ii} - L_i^{n-1}/\lambda_{ii}\right) / \left(\Delta t \dot{u}_i^{n-1/2}\right)$.

The dynamic problem can be solved by the forward difference technique for Eq. (27). The velocity and displacement of the material point when the time step is $n+1$ can be obtained by Eqs. (34) and (35), respectively. The specific calculation flow chart is shown in Fig. 4.

$$\dot{u}_x^{n+1} = \ddot{u}_x^n \Delta t + \dot{u}_x^n \tag{34}$$

$$u_x^{n+1} = \dot{u}_x^{n+1} \Delta t + u_x^n \tag{35}$$

3 Numerical simulation of crack propagation in rock-like materials under tensile load

Rock is a heterogeneous material with a low tensile strength and high compressive strength. It is more prone to failure and damage under a tensile load, than under a compressive load. Hence, the here proposed constitutive model has been used to simulate crack propagation under a biaxial tension in rocks, and to study the influence of different stress ratios on the crack propagation path. The numerical simulation results have in the present study been compared with the results of RFPA [65] to verify the accuracy of the proposed model in this paper. As shown in Fig. 5, there is a flaw with a length of 28 mm in a square rock specimen of size 254 mm × 254 mm, with a flaw inclination angle of 15°. The spacing of material point $\Delta x = 0.001$m, size of horizon $\delta = 3.0\Delta x$, time step size $\Delta t = 5 \times 10^{-8}$, the Young's modulus $E = 47.5$GPa, the density $\rho = 2500$kg/m^3, the tensile strength $f_t = 8.5$MPa and compression strength $f_c = 105$MPa. The critical stretch of the bond in tensile was $s_{2t} = 1.79 \times 10^{-4}$, and the elastic stretch and fracture stretch of the bond in tensile were $s_{1t} = 0.8 s_{2t}$ and $s_t = 5 s_{2t}$, respectively. Furthermore, the critical stretch of the bond in compression was $s_{2c} = 2.21 \times 10^{-3}$, and the elastic stretch and fracture stretch of the bond in compression were $s_{1c} = 0.8 s_{2c}$ and $s_c = 5 s_{2c}$, respectively. The horizontal loads were applied to the left and right sides of the specimen, and the vertical loads were applied to the upper and lower sides of the specimen. Also, the stress loading ratio was described by $B = \sigma_x / \sigma_y$. The values of σ_x, σ_y, and B are shown in Table 1.

Table 1 Loading conditions under different stress ratios

Model	σ_x/MPa	σ_y/MPa	B
1	8.107	6.756	1.2
2	9.1	5.833	1.56
3	9.3	3.72	2.5
4	10.5	3.5	3

Furthermore, the dynamic crack propagation problem was solved by forward and backward difference techniques.

As shown in Fig. 6, the maximum strain energy density was concentrated at the crack tip and moved along the crack propagation path. The crack was initiated at 0.04 ms and propagated along the direction of the maximum principal stress. The final crack propagation path under different loading stress ratios is shown in Fig. 7. With the increase in stress ratio, B, the curvature of the crack increased. Also, the crack growth direction changed from the maximum principal stress direction to the minimum principal stress direction. These numerical simulation results were in good agreement with both the simulation results of RFPA [65] and the experimental results [66]. The validity of the proposed model to simulate the crack propagation under a tensile load has, thereby, been verified.

4 Numerical simulation of crack propagation in rock-like materials under compressive load

4.1 Crack propagation under uniaxial compression

To further verify the validity of the proposed constitutive model of rock-like materials, numerical simulations of a uniaxial compression of rock-like materials have been conducted. According to the work by Yang et al. [57] (Fig. 8), the specimen was simplified into a planar stress problem. The size of the model is 80 mm × 160 mm, the elastic modulus $E = 13.94$GPa and the density $\rho = 2449\text{kg/m}^3$, the tensile strength $f_t = 10$MPa and compression strength $f_c = 117.4$MPa. The critical stretch of the bond in tensile was $s_{2t} = 7.17 \times 10^{-4}$, and the elastic stretch and fracture stretch of the bond in tensile were $s_{1t} = 0.8 s_{2t}$ and $s_t = 7 s_{2t}$, respectively. Also, the critical stretch of the bond in compression was $s_{2c} = 8.42 \times 10^{-3}$, and the elastic stretch and fracture stretch of the bond in compression were $s_{1c} = 0.8 s_{2c}$ and $s_c = 7 s_{2c}$, respectively. Furthermore, the virtual boundary layer was assigned the upper and lower ends of the model, and the thickness of the boundary layer was three times the distance between two material points. A displacement load was applied to the virtual boundary layer at the loading rate of $\pm 5.0 \times 10^{-8}$m/s. The problem of uniaxial compression was solved by the adaptive dynamic relaxation method.

The material point distance and the horizon had an important influence on the crack growth [67]. The δ-convergence and m-convergence (m is the ratio of the horizon to the material point distance) were performed according to the proposed constitutive model (Fig. 9). As can be seen in Fig. 10a, the

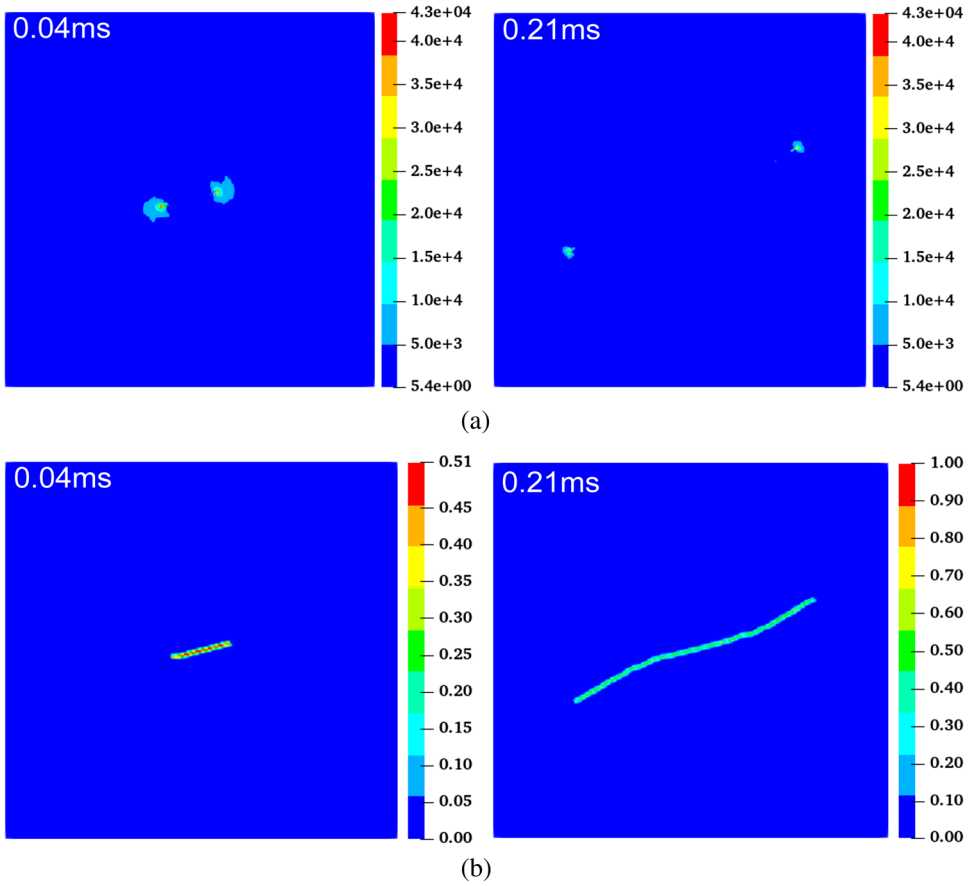

Fig. 6 Contours of strain energy density and crack propagation process at stress ratio $B = 3$. (**a**) Contours of the strain energy density. (**b**) The crack propagation process under biaxial tension

result of the numerical simulations, with a uniaxial compression, was an X-shaped conjugate inclined plane shear failure for different δ and m values, which was one of the most typical failure modes of rocks [68]. When m was fixed, the crack propagation became clearer with a decrease in horizon δ. When δ was fixed, the crack propagation became smoother with an increase in m. It can be seen from the stress-strain curve in Fig. 10b that the present simulation could reflect the deformation stages of pre-peak, peak, and post-peak in the uniaxial compression. The simulated stress-strain curves under different δ and m values were consistent with the stress-strain curves obtained by laboratory tests. However, the computational efficiency decreased with a decrease in δ and an increase in m. Therefore, the optimal value of m was 4 and the optimal value of δ was 2.0 mm.

4.2 Crack initiation and propagation of a single non-straight flaw

As a natural non-homogeneous material, a rock may include non-straight cracks. The propagation and coalescence of non-straight cracks will give rise to a reduction in structural strength, thereby causing serious engineering problems. Consequently, uniaxial compression of rocks with a single non-straight flaw has been simulated numerically, and the geometric and physical parameters of the chosen model were identical to the one present in Section 4.1. For convenience, the "pre-existing crack" is from here on called "flaw" and the "propagation crack" is called "crack". A single non-straight crack of length $L = 30$ mm and of width $b = 2$ mm was formed in the center of the specimen, and the angle between the crack length direction and horizontal line was α(Fig. 11a). The spacing of material point $\Delta x = 0.0005$m, size of horizon $\delta = 4.0\Delta x$. In peridynamic, preforming a flaw requires to break the bond at the centerline where the crack is located. The centerline with a single non-straight flaw at different inclination angles can be expressed by the Eq. (36):

$$\left(y_1 \cos(\alpha) - x_1 \sin(\alpha)\right) = \frac{L}{8} \sin\left(\frac{2\pi}{L}\left(x_1 \cos(\alpha) + y_1 \sin(\alpha)\right)\right) + \frac{b}{2} \tag{36}$$

where, L is the length of pre-existing flaws, α represents the inclination angle of pre-existing flaws and b is the width of flaws.

A comparison between the previous experimental and numerical simulation results of the mechanical parameters and deformation characteristics of the specimen with a single non-straight flaw under uniaxial compression at different inclination angles, is shown in Fig. 11. As can be seen in Fig. 11b, the peak force and post-peak results match well for the experiments [57] and simulations, but there is

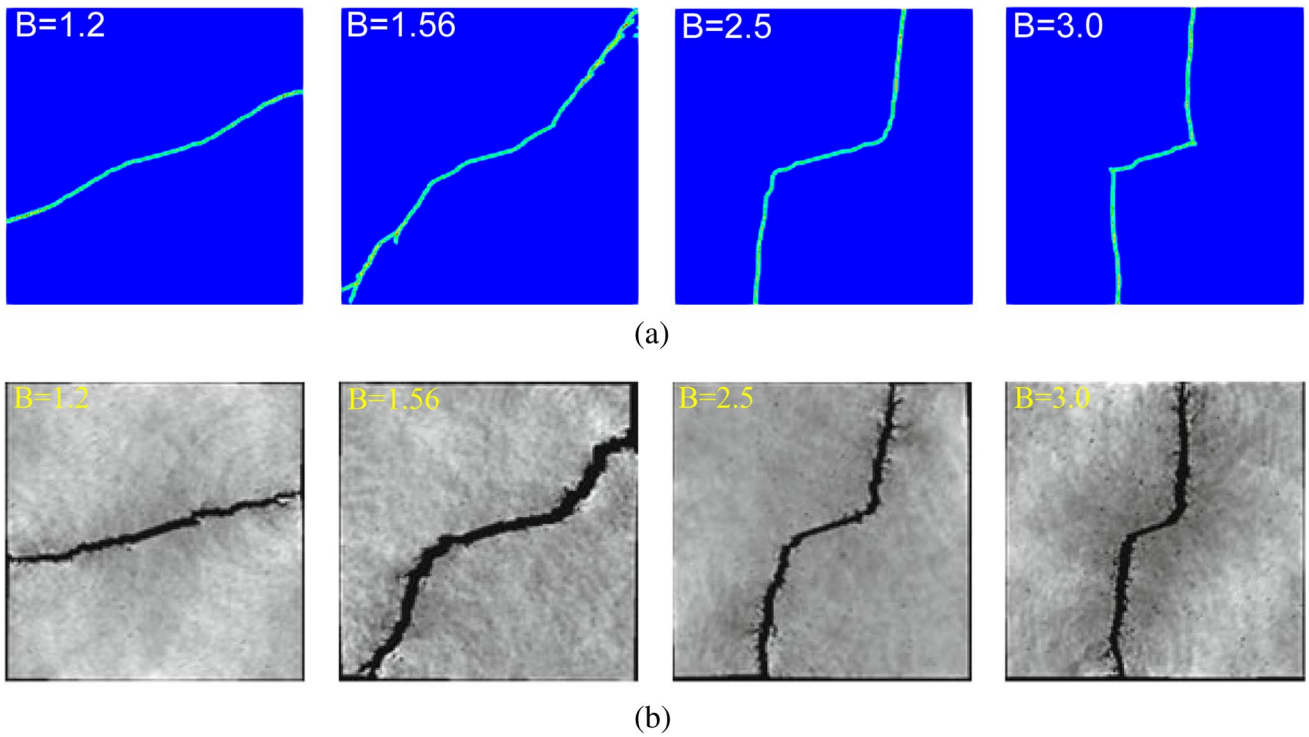

Fig. 7 Comparison of the crack propagation paths obtained from the present simulation and the RFPA simulation [65]. (**a**) Crack propagation paths in present simlation. (**b**) Crack propagation paths by using RFPA

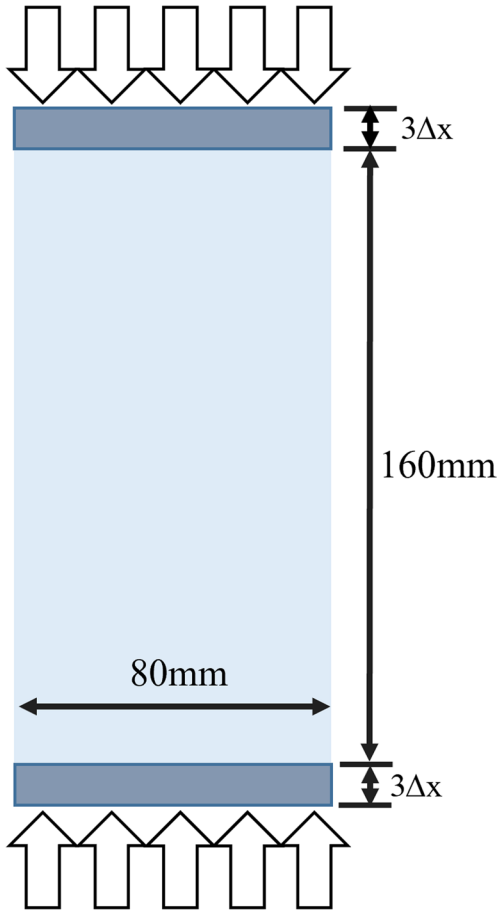

Fig. 8 Numerical model under uniaxial compression

a significant mismatch of the pre-peak results. The reason is that under a compressive load, the internal pores of the rock specimen will gradually close, and the specimen will become more compact, thereby forming an early nonlinear deformation. However, the natural pores in the rock have not been considered in the numerical simulations. As can be seen in Fig. 11c, with an increase in the inclination angle, α, the peak stress obtained from numerical simulation increases, which is consistent with the trend in the experimental results [57]. Moreover, the peak strengths obtained by numerical simulations are very similar to the peak strengths in the experimental results [57]. A comparison of peak strains obtained experimentally and by numerical simulations, for a sample with a single non-straight flaw at different inclination angles, is shown in Fig. 11d. This result shows that the trend in peak strain for the numerical simulation results is consistent with that of the experimental results for an increase in inclination angle. However, the peak strains that are calculated are smaller than the experimentally obtained ones. The reason is that the natural pores in the rock were not taken into consideration in the numerical simulations.

Figure 12 shows the process of crack initiation and propagation with a single non-straight flaw at different inclination angles under uniaxial compression. When load was applied to point A, the tensile cracks 1^a and 1^b were initiated from the convex point of a non-straight flaw in the specimen. Furthermore, when load was applied to point B, the tensile cracks 1^a and 1^b continued to propagate along the loading direction, and tensile cracks 2^a and 2^b started to form at the tip of the pre-existing flaw. When a load was applied to point C, the tensile cracks 1^a and 1^b stopped expanding. Finally, when load was applied to peak point D, the shear cracks 3^a and 3^b became initiated and continued to propagate. In addition, the cracks 2^a, 2^b, 3^a, and 3^b became coalescent through the entire sample.

When load was applied to point A on a sample containing a single non-straight crack with $\alpha = 15^\circ$, the wing tension cracks 1^a and 1^b were initiated from the tip of the pre-existing flaw. As the load continued to increase, the wing tension cracks 1^a and 1^b extended along the vertical direction of the prefabricated flaw for a certain length and then continued to propagate along the loading direction. When load was applied to point B, the tensile crack 2 was initiated from the lower tip of the pre-existing flaw. Furthermore, when load was applied to point C, the secondary shear crack 3 emerged at the upper tip of the pre-existing flaw. Finally, when load was applied to point D, the shear cracks 4^a and 4^b became initiated and propagated. In addition, the cracks 3, 4^a and 4^b became coalescent through the entire specimen.

Figure 12c shows that the load is applied to point A, wing tension cracks 1^a and 1^b emerge at the tip of the prefabricated

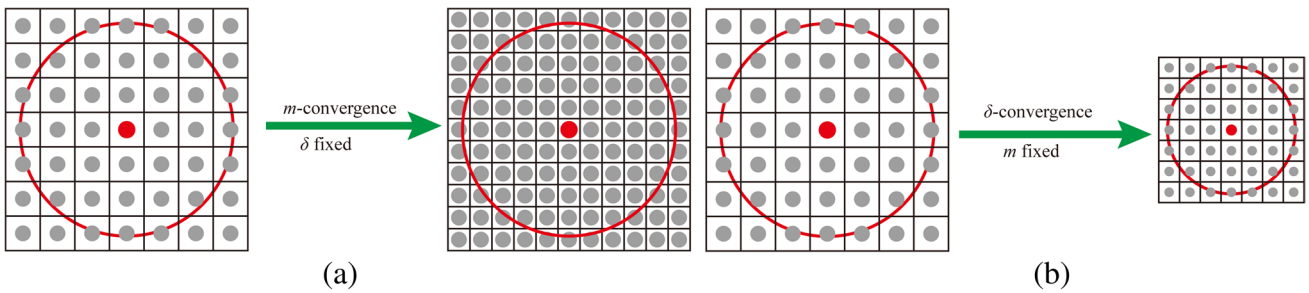

Fig. 9 Diagram of m-convergence and δ-convergence, (**a**) m-convergence, (**b**) δ-convergence

flaw and propagate along the vertical direction of the pre-fabricated flaw. Then the load continues to increase, and the wing tensile cracks 1^a and 1^b extend for a certain length along the vertical direction of the pre-existing flaw and then continued to propagate along the loading direction. When the load increased to point B, the secondary shear crack 2 is initiated from the upper tip of the flaw. As the load continues to increase, the shear crack 3 emerges at the upper tip of the flaw. Finally, when the load increases to point D, secondary shear cracks 2 and 3 coalesce the specimen, and accompany by crack 4.

For the specimen containing a single non-straight flaw with $\alpha = 45^\circ$ loads to point A, the wing cracks 1^a and 1^b are initiated from the tip of the prefabricated flaw. And then when the wing cracks 1^a and 1^b propagate to a certain length along vertical direction of the pre-existing flaw, they gradually propagate along the loading direction. When the load increases to point B, the shear stress at the crack tip increases, and secondary shear crack 2 emerges at the lower tip of the flaw. As the load increase to point C, shear crack 3 is initiated from the upper tip of the flaw. With the increase of load, cracks 4^a, 4^b, 5^a and 5^b initiate and propagate, and ultimately, cracks 2, 3, 5^a and 5^b propagate and coalesce the specimen.

It can be seen from Fig. 12e that when the specimen is loaded to point A, wing cracks 1^a and 1^b are initiated from the tip of the prefabricated flaw. Then, the load continues to increase, and the wing cracks 1^a and 1^b propagate along the loading direction. When the axial stress increases to 65.16 MPa, secondary shear crack 2 initiate from the upper tip of the prefabricated flaw. In pace with the increase to point C of load, secondary shear crack 3 is initiated at the lower tip of the prefabricated flaw. As the load is loaded to peak point D, shear cracks 4^a and 4^b initiate and propagate, and ultimately, cracks 2, 3, 4^a and 4^b coalesce through the specimen.

When the specimen containing a single non-straight crack with $\alpha = 75^\circ$ is loaded to point A, shear crack 1 is initiated

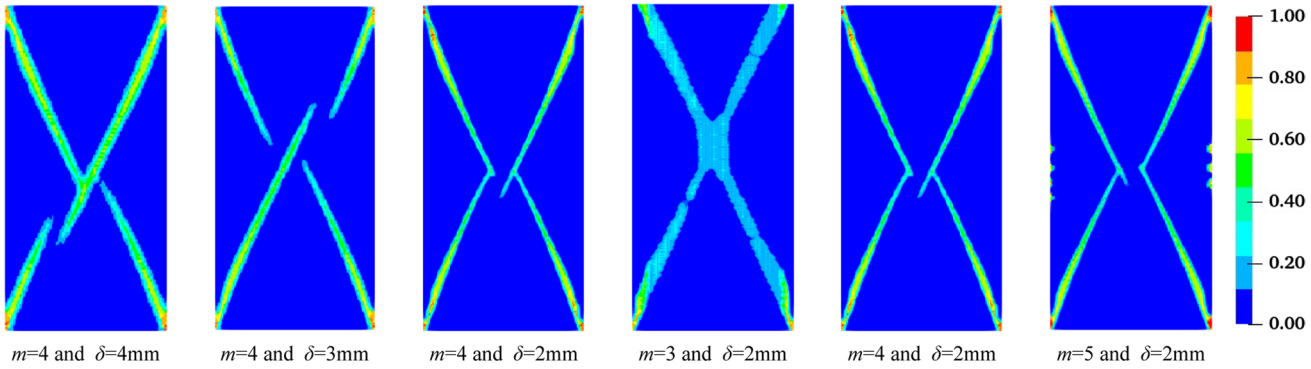

(a)

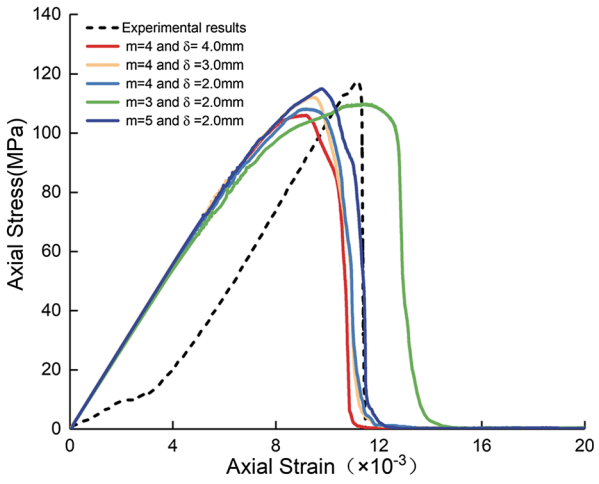

(b)

Fig. 10 Comparison of uniaxial compression experiment [57] and numerical simulation results. (**a**) Crack propagation path under uniaxial compression. (**b**) Stress-strain curve under uniaxial compression

from the non-tip of the prefabricated flaw. In pace with the increase of load, shear crack 2 is initiated at the non-tip of the pre-existing flaw. With the axial stress increases to 84.96 MPa, shear cracks 3^a and 3^b is initiated at the non-tip of the pre-existing flaw. Finally, when the load reaches the peak point D, shear cracks 1, 2, 3^a and 3^b coalesce through the specimen.

For the specimen containing a single non-straight flaw with $\alpha = 90^{\circ}$, when the load is loaded to point A, shear cracks 1^a and 1^b are initiated at the non-tip of the pre-existing flaw. With the increase of load, shear crack 2 is initiated at the convex point of the prefabricated flaw. When the axial stress increases to 83.32 MPa, shear crack 3 is initiated at the convex point of the prefabricated flaw. When loading the specimen to failure, shear cracks 2, 3, 4^a and 4^b propagate and coalesce through the specimen, and the specimen finally showed X-shaped shear failure, similar to uniaxial compression.

Figure 13 shows the comparison between the present simulations and previous experimental results [57] for the initial crack growth with a single non-straight flaw under different inclination angles α. The results from the numerical simulations showed that when α= 15°, 30°, 45°, and 60°, the crack initiated from the tip of the pre-existing flaw, and when α= 0 °, 75 °, and 90 °, the crack initiated from another place of the pre-existing flaw. Compared with the previous experimental results [57], the crack initiation position that was obtained by using the proposed constitutive model was consistent with the experimental results.

From the numerical simulation results in Fig. 14, it could be concluded that the proposed constitutive model could simulate the initiation and propagation of wing cracks, secondary cracks, tensile cracks, and shear cracks. Thus, these cracks were similar to the experimentally obtained ones [57]. However, there were some differences between the numerical simulations and the

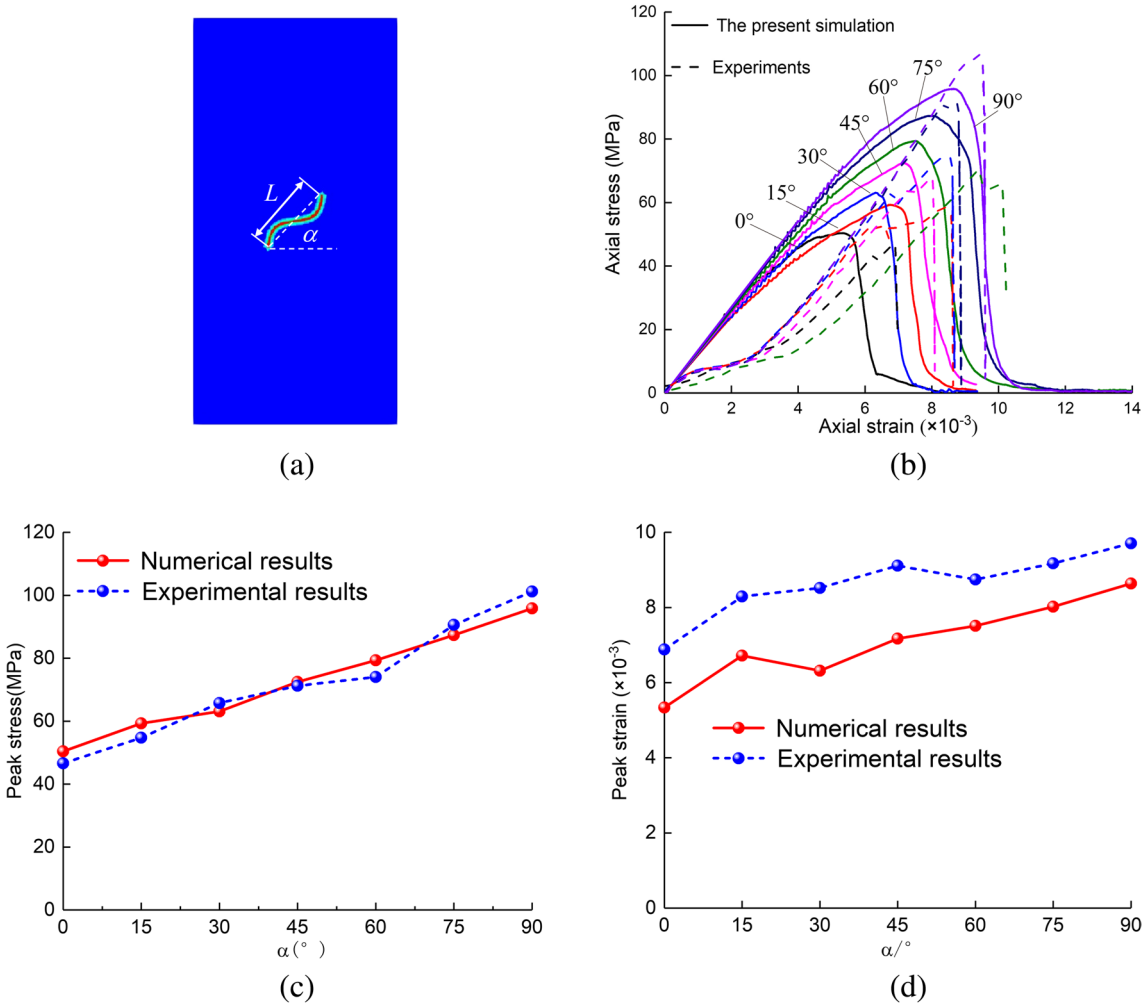

Fig. 11 Comparison between present simulation and experiment results [57] of single non-straight flaw specimen under uniaxial compression. (**a**) Numerical model of specimen containing single non-straight flaw. (**b**) Stress-strain curves. (**c**) Peak stress and (**d**) Peak strain

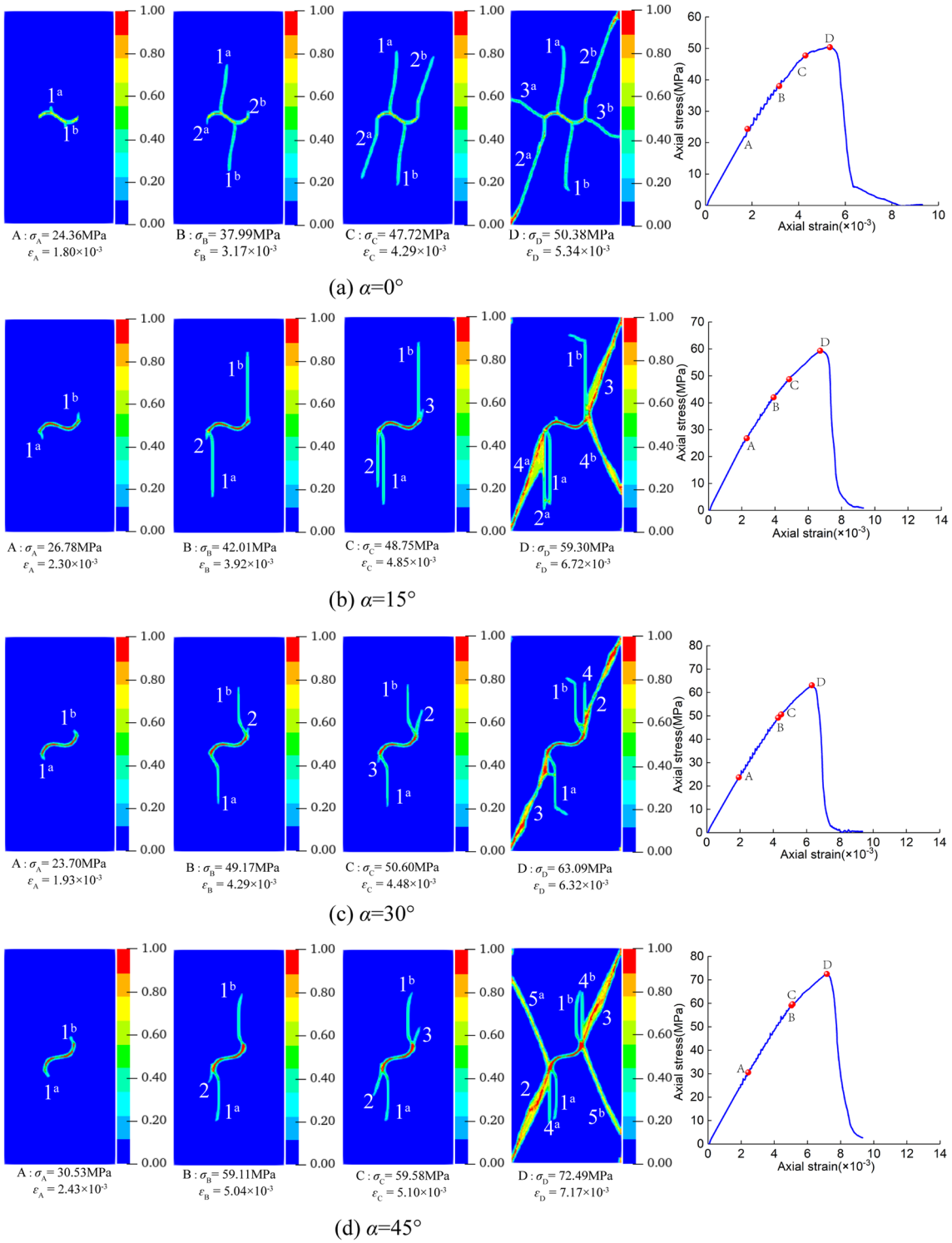

Fig. 12 Crack growth process and stress-strain curve of single pre-existing non-straight flaw under different inclination angles. (**a**) $\alpha = 0°$ (**b**) $\alpha = 15°$ (**c**) $\alpha = 30°$ (**d**) $\alpha = 45°$ (**e**) $\alpha = 60°$ (**f**) $\alpha = 75°$ (**g**) $\alpha = 90°$

experimental results, which may be due to the heterogeneity and processing errors of the samples. According to the comparisons and conclusions above, it could be seen that the results obtained from the proposed constitutive model were basically consistent with the experimental results, regardless of strength characteristics, deformation characteristics, and crack growth processes. This verifies the feasibility of the proposed model in the prediction of

crack propagation, strength characteristics, and deformation characteristics.

4.3 Crack propagation and coalescence of three pre-existing flaws

Yang et al. [8] studied the mechanical properties and crack propagation characteristics of sandstone, with three pre-existing flaws, by using an experimental method. We have used the same geometric model as Yang et al. [8] in their experiment, and the size of the model was 80 mm × 160 mm. As shown in Fig. 15, the length of the pre-existing flaw was $2a$, and the inclination angle was β. Also, the length of the ligament between the flaw ① and flaw ② was $2b$, and the ligament inclination was α. Furthermore, the ligament length between flaw ② and flaw ③ was $2c$, and the inclination angle of the ligament was β_1. The flaws ①, ② and ③ were situated in parallel with each other and the flaws ① and ② were coplanar. The geometric parameters of the pre-existing three flaws are shown in Table 2.

To simulate the crack propagation process of the pre-existing three flaws in the sandstone under uniaxial compression, it was simplified to a planar stress problem. The sandstone was discretized into $160 \times 320 = 51200$ points. The distance between the material points was $\Delta x = 0.5$mm and the size of the horizon was $\delta = 4\Delta x$. In addition, the material properties were selected from the experiments: Young's modulus $E = 26.7$GPa, Poisson's ratio $\nu = 0.33$, mass density $\rho = 2650$kg/m^3, the tensile strength $f_t = 12$MPa and compression strength $f_c = 190.8$MPa. The critical stretch of the bond in tensile was $s_{2t} = 4.49 \times 10^{-4}$, and the elastic stretch and fracture stretch of the bond in tensile were $s_{1t} = 0.8s_{2t}$ and $s_t = 10s_{2t}$, respectively. The critical stretch of the bond in compression was

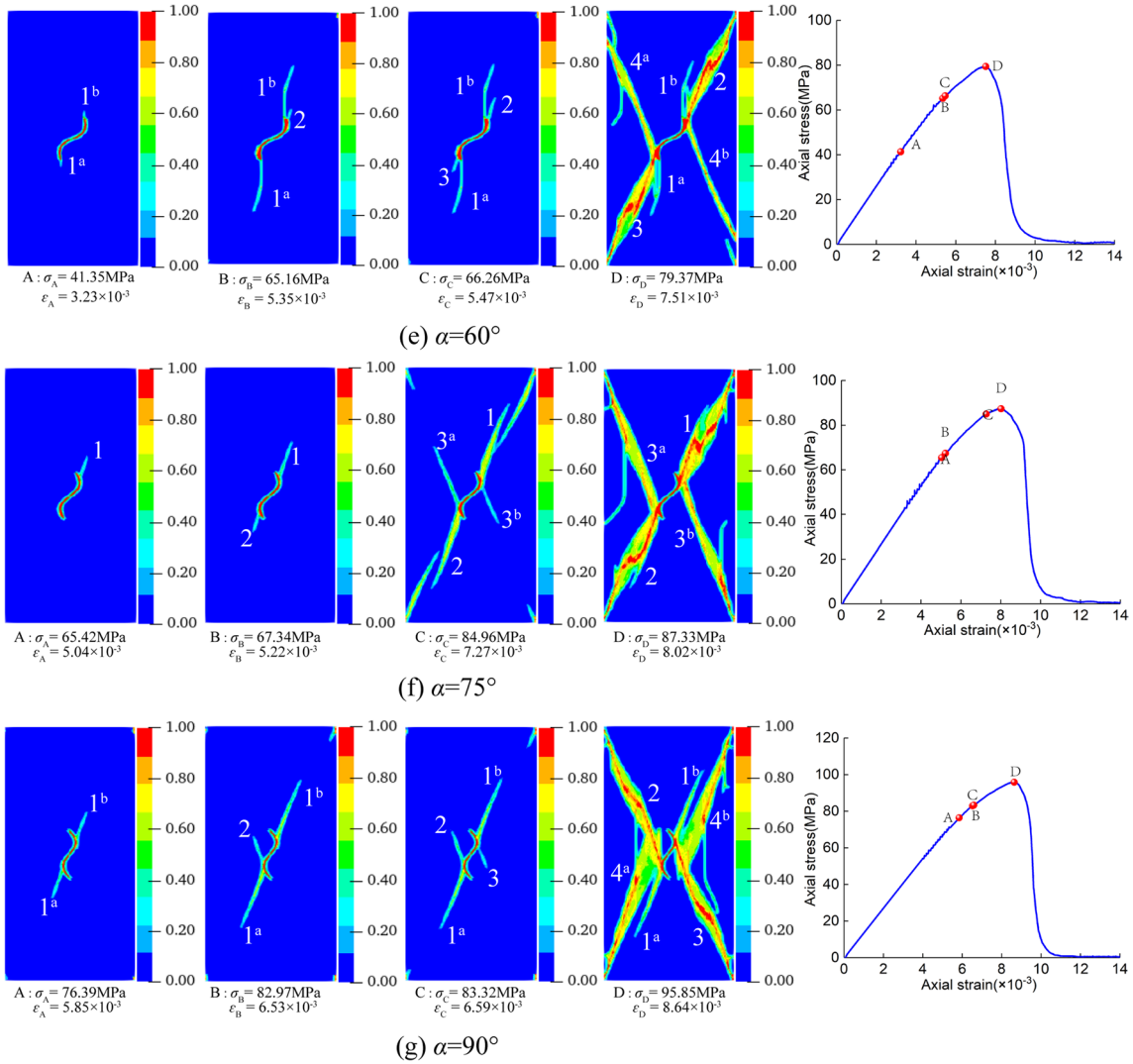

Fig. 12 (continued)

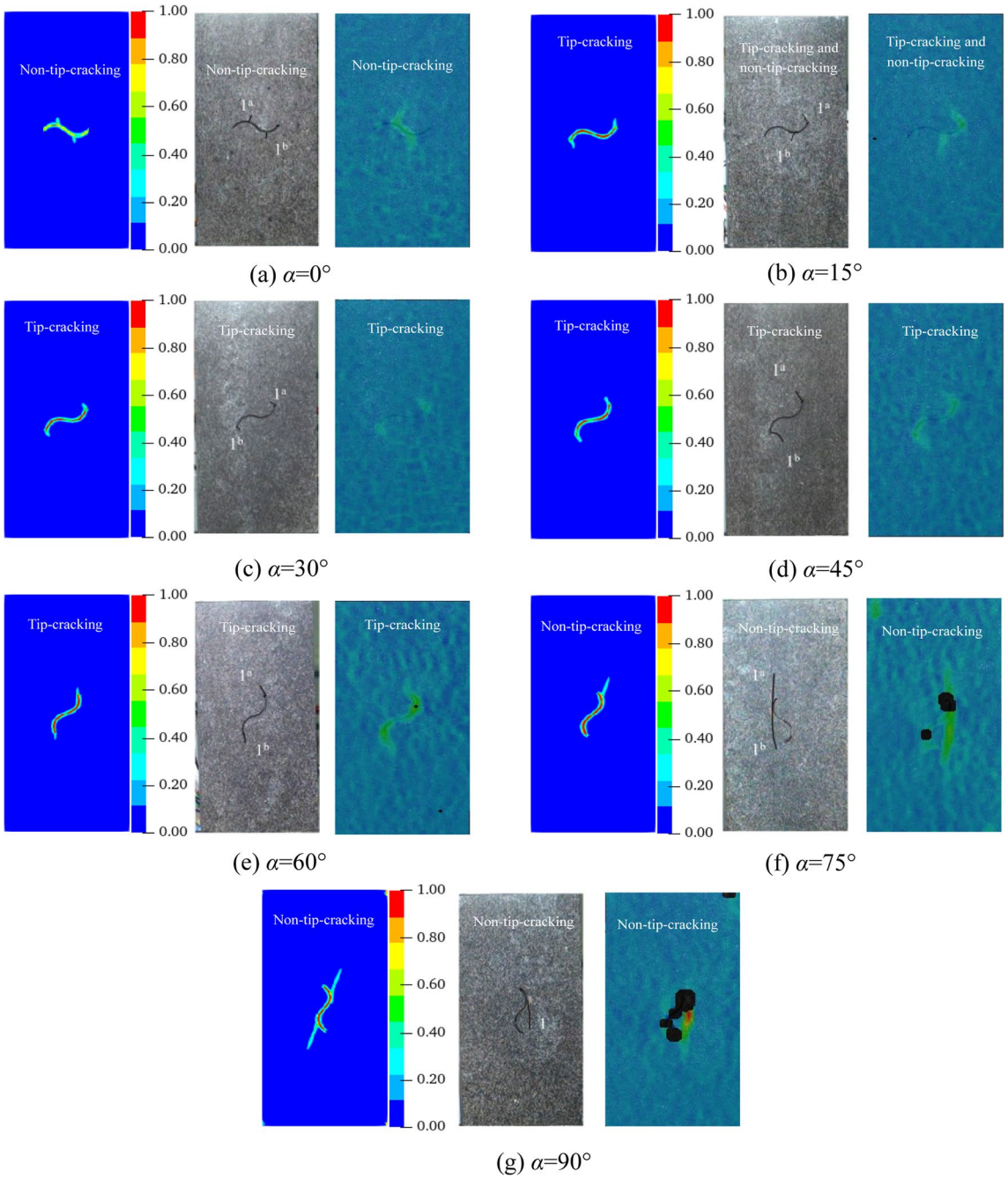

Fig. 13 Comparison of the initial crack growth paths in the specimen containing a single pre-existing flaws with the different inclination angle α obtained from the proposed model and the previous experimental results [57]. (**a**) $\alpha = 0°$ (**b**) $\alpha = 15°$ (**c**) $\alpha = 30°$ (**d**) $\alpha = 45°$ (**e**) $\alpha = 60°$ (**f**) $\alpha = 75°$ (**g**) $\alpha = 90°$

$s_{2c} = -7.14 \times 10^{-3}$, and the elastic stretch and fracture stretch of the bond in compression were $s_{1c} = 0.8 s_{2c}$ and $s_c = 10 s_{2c}$, respectively. Furthermore, the virtual boundary layer was defined by the upper and lower ends of the model, and the thickness of the boundary layer was three times as long as the spacing between two material points. Also, the displacement load was applied to the virtual boundary layer at the loading rate of $\pm 5.0 \times 10^{-8}$m/s, and the adaptive dynamic relaxation method was used to solve the quasi-static problem.

It could be observed that as the load increased, wing cracks were initiated from the inner and outer tips of the pre-existing flaws (Fig. 16). When the wing cracks continued to propagate along the direction of the maximum principal stress, the flaws ② and ③ became coalescent (Fig. 16b). Furthermore, when the axial stress increased

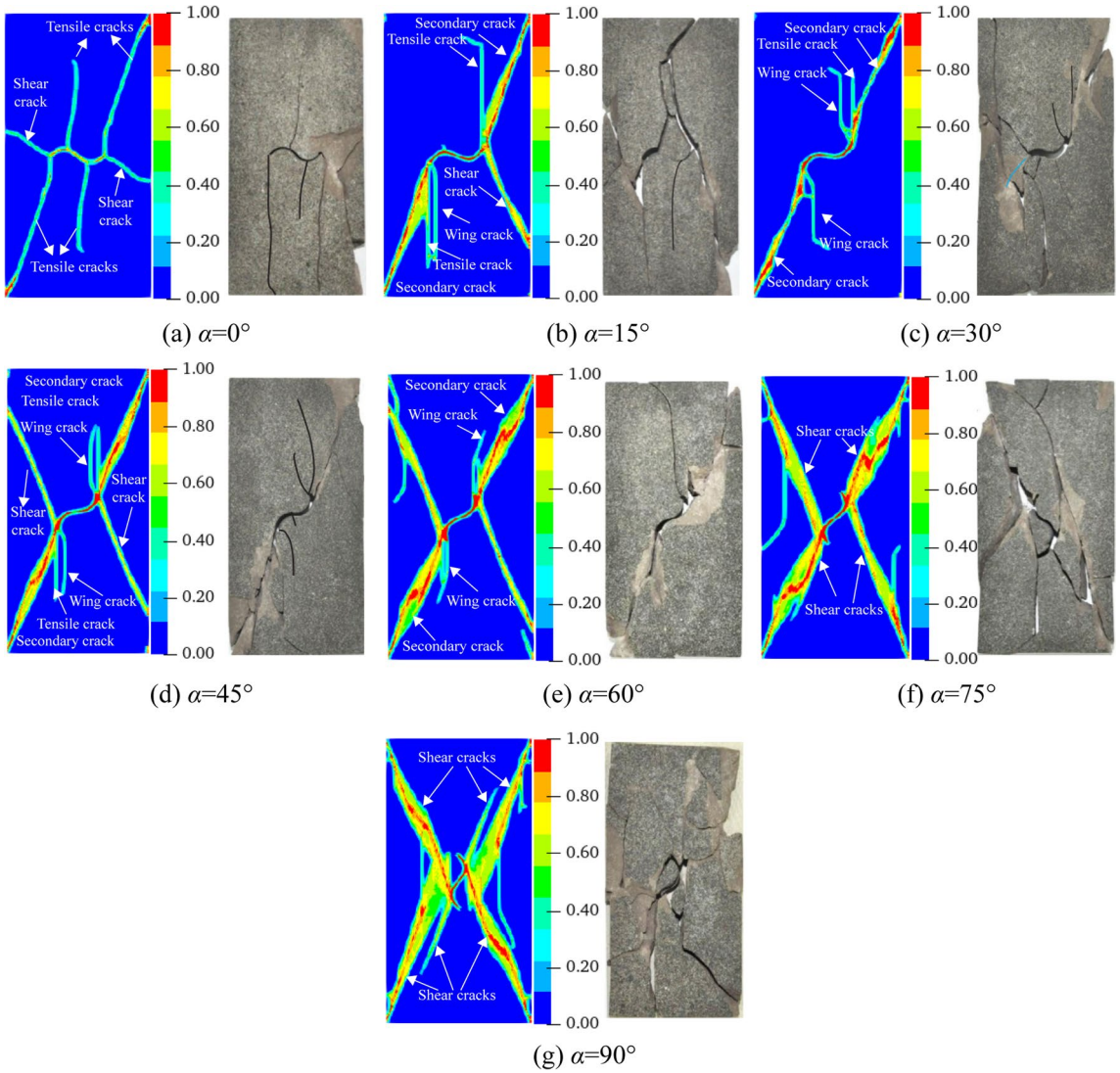

Fig. 14 Comparison of the crack propagation paths in the specimen containing a single pre-existing flaws with the different inclination angle α obtained from the present simulation and the previous experimental results [57]. (**a**) $\alpha = 0°$ (**b**) $\alpha = 15°$ (**c**) $\alpha = 30°$ (**d**) $\alpha = 45°$ (**e**) $\alpha = 60°$ (**f**) $\alpha = 75°$ (**g**) $\alpha = 90°$

to 86.46 MPa, the anti-wing crack that emerged from the inner tip of flaw ① coalesced with the anti-wing crack that was initiated from the outer tip of flaw ③. Finally, the anti-wing crack that emanated from the outer tip of flaw ①, and the wing crack that initiated from the outer tip of flaw ②, propagated and became coalescent through the whole sample.

Figure 17 shows the crack growth process with the ligament angle $\beta_1 = 90^{\circ}$. In pace with the increase of load, wing crack initiate from the inner and outer tips of flaws ①, ② and ③. When the axial stress increases to 58.84 MPa, flaws ② and ③ are coalesced. With the continuous increase of load, the oblique secondary crack emerges from the inner tip of flaw ① coalesce with the oblique secondary crack initiate from the outer tip of flaw ②. With the load increasing to 79.85 MPa, quasi-coplanar secondary crack and anti-wing crack initiate from the outer tip of flaw ① and wing crack emanates from the outer tip of flaw ② propagate, and the crack coalesce through specimen.

It can be observed from Fig. 18 that wing crack first emanate from the inner and outer tips of flaws ①, ②, and ③. Then, as the load continues to increase, the oblique secondary crack initiate from the inner tip of the flaw ① coalesce with the oblique secondary crack initiate from the outer tip of the crack ③. At this time, the crack propagation mode is different from that of the ligament angle $\beta_1 = 75^{\circ}$ and $\beta_1 = 90^{\circ}$. When the load continues to increase to 84.67 MPa, the wing crack emanates from the inner tip of flaw ② and the wing crack emerges from the outer tip of flaw ③ are coalesced through. The anti-wing crack and quasi-coplanar secondary crack initiate from the outer tips of flaws ① and the wing crack

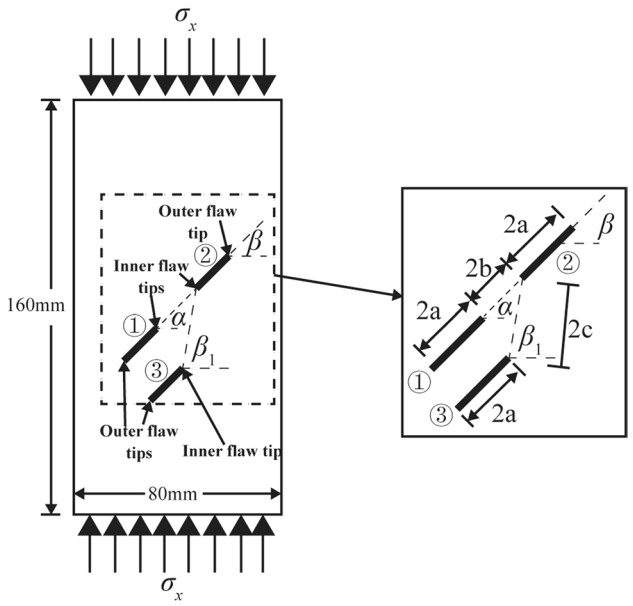

Fig. 15 Numerical model of pre-existing three flaws specimen

emanates from the outer tip of flaw ② further propagate until the load increases to 98.32 MPa, and the cracks coalesce through the specimen.

Figure 19 shows the crack propagation process with the ligament angle $\beta_1 = 120^{\circ}$. It can be seen from Fig. 19 that wing cracks first initiate from the inner and outer tips of the flaw ①, and the outer tips of the flaws ② and ③. Then, with the increase of load, the oblique secondary crack emerges from the inner tip of flaw ① is coalesced with the oblique secondary crack initiate from the outer tip of flaw ③, and the quasi-coplanar secondary cracks is initiated from the inner tip of flaw ①. When the load increases to 86.39 MPa, the initiated quasi-coplanar secondary crack at the inner tip of flaw ② is coalesced with the crack between ligament of flaws ① and ③. Then, the initiated quasi-coplanar secondary crack and oblique secondary crack at the outer tips of flaws ① and the wing crack emanates from the outer tip of flaw ③ continued to propagate until the load increased to 101.53 MPa, and the crack coalesces through the specimen.

The crack coalescence patterns of the red sandstone specimen containing pre-existing three flaws is related to the ligament angle β_1. The coalescence pattern in the ligament region falls into two types (Fig. 20a). The coalescence of anti-wing cracks is first type, and the other type is the coalescence of wing crack and oblique secondary crack. For the ligament angle $\beta_1 = 75^{\circ}$, flaws ① and ③, flaw ② and ③ are coalesced, while flaws ① and ② are not coalesced.

The crack coalescence patterns of ligament angle $\beta_1 = 90^{\circ}$ is shown in Fig. 20 (b). It can be seen from the figure that the coalescence pattern in the ligament region divided into two types, one is the coalescence of anti-wing cracks and the other is the coalescence of wing crack and oblique secondary crack. For the ligament angle $\beta_1 = 90^{\circ}$, flaws ① and ③, flaw ② and ③ are coalesced, while flaws ① and ② are not coalesced.

Figure 20c shows the crack coalescence patterns of ligament angle $\beta_1 = 105^{\circ}$. It can be seen from the figure that the coalescence pattern in the ligament region have two types. The coalescence of oblique secondary cracks is first type and the other type is the coalescence of wing cracks. For the ligament angle $\beta_1 = 105^{\circ}$, like the above two specimens, flaws ① and ③, flaw ② and ③ are coalesced, while flaws ① and ② are not coalesced.

It can be seen from the Fig. 20d that the coalescence patterns in the ligament region divided into three types, including the coalescence of oblique secondary crack and quasi-coplanar secondary crack, the coalescence of wing crack and quasi-coplanar secondary crack and the coalescence of oblique secondary cracks. Flaws ① and ③, flaw ② and ③ and flaws ① and ② are coalesced in the ligament angle $\beta_1 = 120^{\circ}$ of red sandstone specimen containing three pre-existing flaws.

A comparison of crack propagation paths, that have been obtained from the here proposed constitutive model of rock-like materials, and previous experimental results is shown as Fig. 20. The results indicate that the numerical simulation can well simulate the propagation and coalescence of wing cracks, anti-wing cracks, oblique secondary cracks, and quasi-coplanar secondary cracks, which is in agreement with previous results [8]. As obtained from the numerical simulations, stress-strain curves with the ligament angle β_1 are shown in Fig. 21. When the angle of the ligament increases, the stress peak value first decreases and then increases, which is the same as for previous experimental results [8] and numerical simulation results [48].

Table 2 Geometric distribution parameters of pre-existing three flaws specimens

Specimen	$\alpha(^{\circ})$	$\beta(^{\circ})$	$\beta_1(^{\circ})$	2*a* (mm)	2*b* (mm)	2*c* (mm)
1	45	45	75	15	20	20
2	45	45	90	15	20	20
3	45	45	105	15	20	20
4	45	45	120	15	20	20

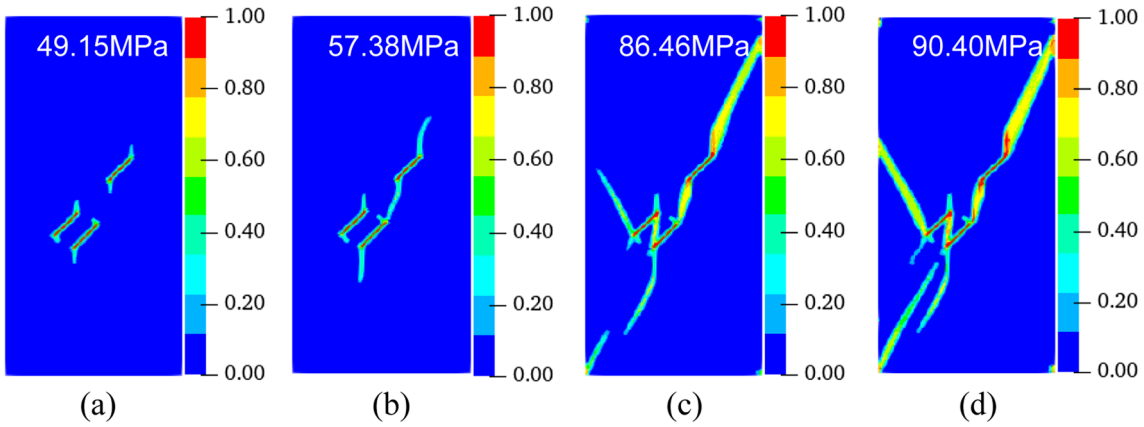

Fig. 16 The process of crack growth with the ligament angle $\beta_1 = 75^{\circ}$. (**a**) $\sigma_x = 49.15$ MPa (**b**) $\sigma_x = 57.38$ MPa (**c**) $\sigma_x = 86.46$ MPa (**d**) $\sigma_x = 90.40$ MPa

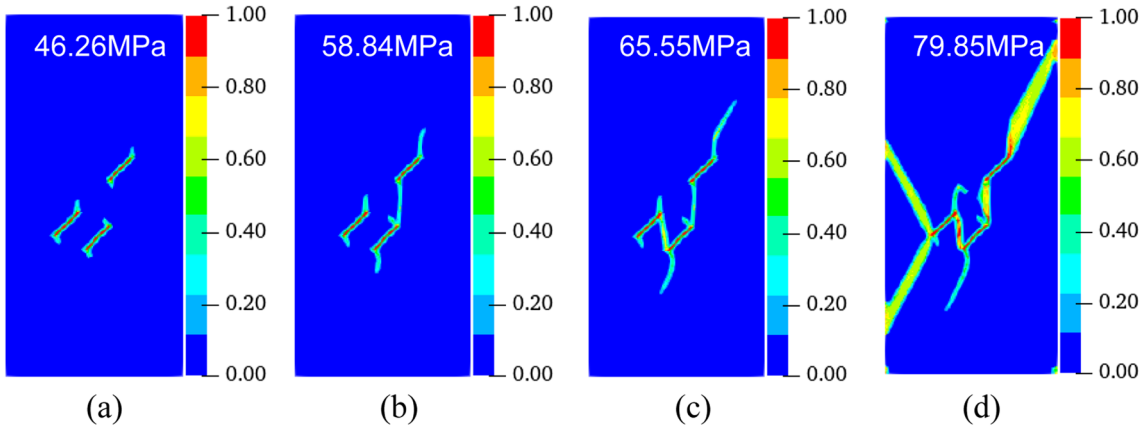

Fig. 17 The process of crack growth with the ligament angle $\beta_1 = 90^{\circ}$. (**a**) $\sigma_x = 46.26$ MPa (**b**) $\sigma_x = 58.84$ MPa (**c**) $\sigma_x = 65.55$ MPa (**d**) $\sigma_x = 79.85$ MPa

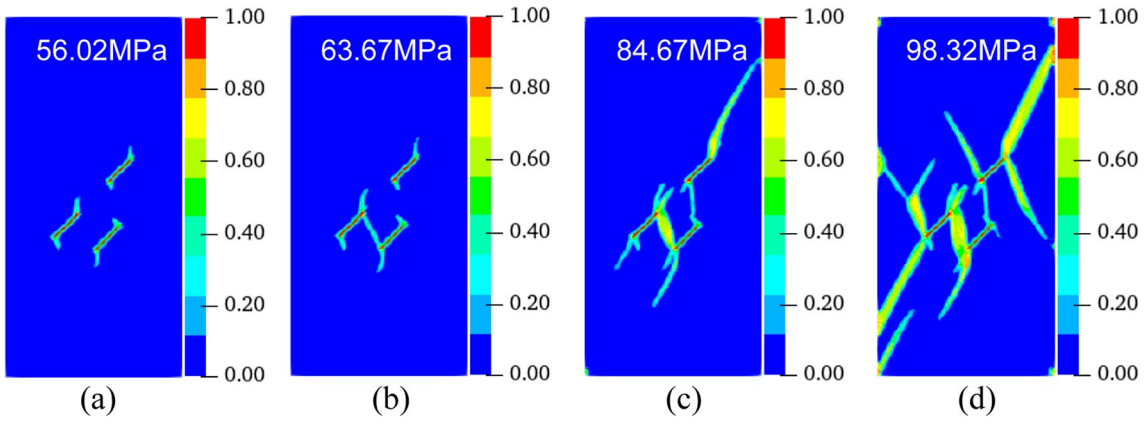

Fig. 18 The process of crack growth with the ligament angle $\beta_1 = 105^{\circ}$. (**a**) $\sigma_x = 56.02$ MPa (**b**) $\sigma_x = 63.67$ MPa (**c**) $\sigma_x = 84.67$ MPa (**d**) $\sigma_x = 98.32$ MPa

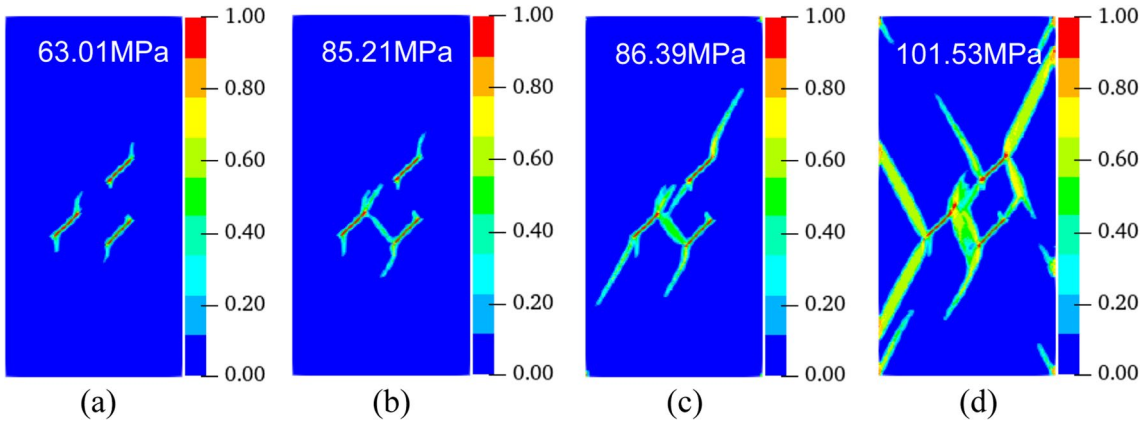

Fig. 19 The process of crack growth with the ligament angle $\beta_1 = 120^{\circ}$. (**a**) σ_x = 63.01 MPa (**b**) σ_x = 85.21 MPa (**c**) σ_x = 86.39 MPa (**d**) σ_x = 101.53 MPa

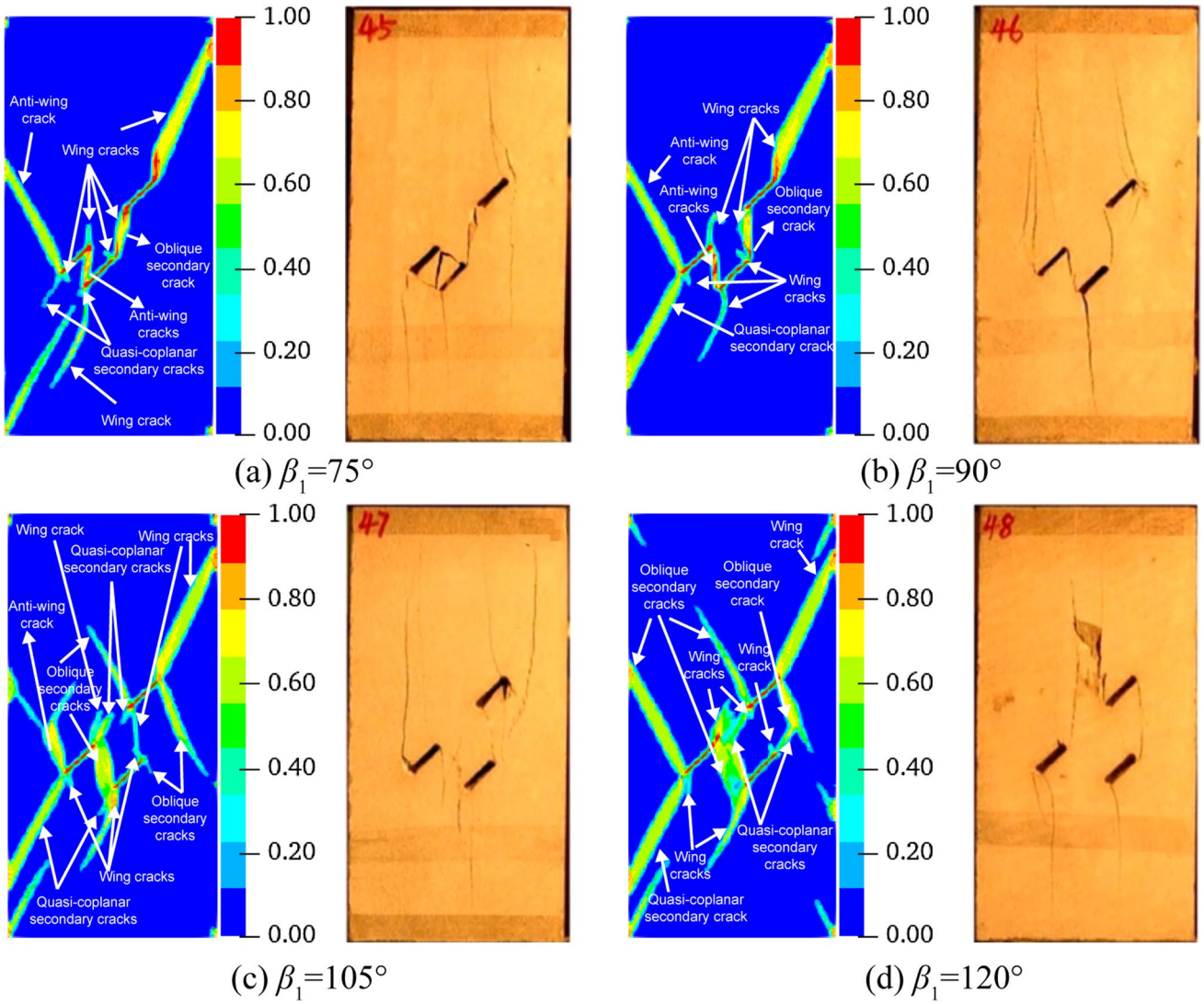

Fig. 20 Comparison between numerical simulation and experimental results [8] of the crack coalescence mode of red sandstone samples containing pre-existing three flaw with ligament angle β_1. (**a**) $\beta_1 = 75°$ (**b**) $\beta_1 = 90°$ (**c**) $\beta_1 = 105°$ (**d**) $\beta_1 = 120°$

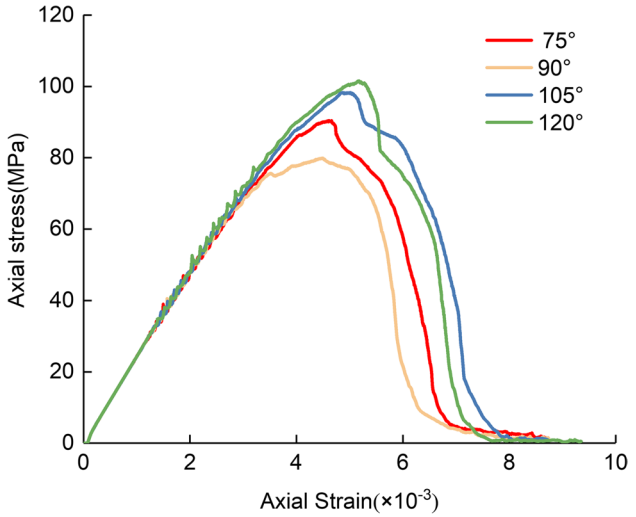

Fig. 21 Stress-strain curves for numerical simulation of pre-existing three flaw specimens with ligament angles β_1

5 Conclusion

In the present study, a constitutive model of rock-like materials has been proposed and the strain energy density has been derived. Also, the model constants, with respect to the elasticity moduli for plane stress conditions, have been obtained by a comparison with the classical elasticity theory. Furthermore, the process of crack initiation, propagation, and penetration under plane stress scenarios, have been simulated. The main conclusions were as follows:

(1) For a rock-like sample with a pre-existing flaw under a biaxial tensile load, the results of numerical simulation showed that with an increase in stress ratio B, the crack curvature increased and the crack propagation direction changed from the maximum principal stress direction to the minimum principal stress direction. It was found that the proposed constitution model could well simulate the crack growth process of rock-like materials under a biaxial tensile load.

(2) The effect of flaw inclination angle on crack propagation in rock-like samples, containing one single non-straight pre-existing flaw under uniaxial compression, has been studied. The numerical simulation results showed that the crack initiation position fell into two types. One was tip-cracking and the other was non-tip-cracking. The crack initiation position was related to inclination angle. When α= 15 °, 30 °, 45 ° and 60 °, the crack initiated from the tip of the pre-existing flaw. When α= 0 °, 75 ° and 90 °, the crack initiated from the non-tip (i.e., from another position than the tip) of the pre-existing flaw. With the increase in the inclination angle, the peak stress of the sample gradually increased. The peak strain of the sample first increased, then decreased, and finally increased again. Moreover, it could be seen that the present numerical simulation results were consistent with the experimental results.

(3) The numerical results of the crack propagation and coalescence in rock-like material samples, with three pre-existing flaws, were in good agreement with the experimental results. The coalescence patterns in the ligament region were relevant to the ligament angle, β_1, and were divided into six types: coalescence of anti-wing cracks, coalescence of wing cracks, coalescence of oblique secondary cracks, coalescence of an oblique secondary crack and wing crack, coalescence of a quasi-coplanar secondary crack and an oblique secondary crack, and coalescence of a wing crack and a quasi-coplanar secondary crack. For β_1=75°, 90°, and 120°, the flaw pairs ①/③ and ②/③ succeeded to coalesce, while the flaw pair ①/② failed to coalesce. Furthermore, the flaw pairs ①/③, ②/③, and ①/② became coalesced for the ligament angle $\beta_1 = 120^{\circ}$ in the rock-like material sample that contained three pre-existing flaws.

Acknowledgements This research is financially supported by National Natural Science Foundation of China (Grant No. 51974187), Natural Science Foundation of Liaoning Province (Grant No. 2019-MS-242), Liaoning Provincial Education Department focuses on tackling key problems (Grant No. LZGD2020004), which are gratefully acknowledgement.

Data availability The datasets generated during the current study are available from the corresponding author on reasonable request.

Declarations

Conflict of interests Authors declare that they have no known competing financial interests or personal relationships that could have appeared to influence the work reported in this paper.

References

1. Bobet, A.: The initiation of secondary cracks in compression. Eng. Fract. Mech. **66**, 187–219 (2000)
2. Li, Y.P., Chen, L.Z., Wang, Y.H.: Experimental research on pre-cracked marble under compression. Int. J. Solids Struct. **42**, 2505–2516 (2005)
3. Wong, L.N.Y., Einstein, H.H.: Crack Coalescence in Molded Gypsum and Carrara Marble: Part 1. Macroscopic Observations and Interpretation. Rock Mech. Rock. Eng. **42**, 475–511 (2008)
4. Yang, S.Q., Jing, H.W.: Strength failure and crack coalescence behavior of brittle sandstone samples containing a single fissure under uniaxial compression. Int. J. Fract. **168**, 227–250 (2010)
5. Yang, L., Jiang, Y.J., Li, B., et al.: Application of the expanded distinct element method for the study of crack growth in rock-like materials under uniaxial compression. Front. Struct. Civ. Eng. **6**, 121–131 (2012)
6. Jin, J., Cao, P., Chen, Y., et al.: Influence of single flaw on the failure process and energy mechanics of rock-like material. Comput. Geotech. **86**, 150–162 (2017)
7. Mughieda, O., Omar, M.T.: Stress Analysis for Rock Mass Failure with Offset Joints. Geotech. Geol. Eng. **26**, 543–552 (2008)
8. Yang, S.Q., Yang, D.S., Jing, H.W., et al.: An Experimental Study of the Fracture Coalescence Behaviour of Brittle Sandstone

Specimens Containing Three Fissures. Rock Mech. Rock. Eng. **45**, 563–582 (2011)
9. Yang, S.Q., Liu, X.R., Jing, H.W.: Experimental investigation on fracture coalescence behavior of red sandstone containing two unparallel fissures under uniaxial compression. Int. J. Rock. Mech. Min. **63**, 82–92 (2013)
10. Zhou, X.P., Cheng, H., Feng, Y.F.: An Experimental Study of Crack Coalescence Behaviour in Rock-Like Materials Containing Multiple Flaws Under Uniaxial Compression. Rock Mech. Rock. Eng. **47**, 1961–1986 (2013)
11. Cao, P., Liu, T.Y., Pu, C.Z., et al.: Crack propagation and coalescence of brittle rock-like specimens with pre-existing cracks in compression. Eng. Geol. **187**, 113–121 (2015)
12. Watwood, V.B.: The finite element method for prediction of crack behavior. Nucl. Eng. Des. **11**, 323–332 (1970)
13. Mergheim, J., Kuhl, E., Steinmann, P.: A finite element method for the computational modelling of cohesive cracks. Int. J. Numer. Meth. Eng. **63**, 276–289 (2005)
14. Zhou, Q., Zhu, Z.M., Wang, X., et al.: The effect of a pre-existing crack on a running crack in brittle material under dynamic loads. Fatigue. Fract. Eng. M. **42**, 2544–2557 (2019)
15. Zhou, L., Zhu, Z.M., Dong, Y.Q., et al.: Investigation of dynamic fracture properties of multi-crack tunnel samples under impact loads. Theor. Appl. Fract. Mec. **109**, 102733 (2020)
16. Haeri, H., Shahriar, K., Marji, M.F., et al.: Experimental and numerical study of crack propagation and coalescence in pre-cracked rock-like disks. Int. J. Rock. Mech. Min. **67**, 20–28 (2014)
17. Areias, P.M.A., Belytschko, T.: Analysis of three-dimensional crack initiation and propagation using the extended finite element method. Int. J. Numer. Meth. Eng. **63**, 760–788 (2005)
18. Mohtarami, E., Baghbanan, A., Hashemolhosseini, H., et al.: Fracture mechanism simulation of inhomogeneous anisotropic rocks by extended finite element method. Theor. Appl. Fract. Mec. **104**, 102359 (2019)
19. Surendran, M., Natarajan, S., Palani, G.S., et al.: Linear smoothed extended finite element method for fatigue crack growth simulations. Eng. Fract. Mech. **206**, 551–564 (2019)
20. Wu, Z.J., Wong, L.N.Y., Fan, L.F.: Dynamic Study on Fracture Problems in Viscoelastic Sedimentary Rocks Using the Numerical Manifold Method. Rock Mech. Rock. Eng. **46**, 1415–1427 (2013)
21. Wong, L.N.Y., Wu, Z.: Application of the numerical manifold method to model progressive failure in rock slopes. Eng. Fract. Mech. **119**, 1–20 (2014)
22. Zhang, Z.S., Wang, S.H., Wang, C.G., et al.: A study on rock mass crack propagation and coalescence simulation based on improved numerical manifold method (NMM). Geomech. Geophys. Geo. **7**, 1–16 (2020)
23. Ning, Y.J., Yang, J., An, X.M., et al.: Simulation of blast induced crater in jointed rock mass by discontinuous deformation analysis method. Front. Archit. Civ. Eng. China. **4**, 223–232 (2010)
24. He, P., Li, S.C., Li, L.P., et al.: Discontinuous deformation analysis of super section tunnel surrounding rock stability based on joint distribution simulation. Comput. Geotech. **91**, 218–229 (2017)
25. Yang, S.Q., Tian, W.L., Huang, Y.H., et al.: Experimental and discrete element modeling on cracking behavior of sandstone containing a single oval flaw under uniaxial compression. Eng. Fract. Mech. **194**, 154–174 (2018)
26. Lin, Q.B., Cao, P., Meng, J.J., et al.: Strength and failure characteristics of jointed rock mass with double circular holes under uniaxial compression: Insights from discrete element method modelling. Theor. Appl. Fract. Mec. **109**, 102692 (2020)
27. Ning, Y.J., An, X.M., Ma, G.W.: Footwall slope stability analysis with the numerical manifold method. Int. J. Rock. Mech. Min. **48**, 964–975 (2011)
28. Silling, S.A.: Reformulation of elasticity theory for discontinuities and long-range forces. J. Mech. Phys. Solids. **48**, 175–209 (2000)
29. Huang, D., Lu, G.D., Wang, C.W., et al.: An extended peridynamic approach for deformation and fracture analysis. Eng. Fract. Mech. **141**, 196–211 (2015)
30. Wan, J., Chen, Z., Chu, X.H., et al.: Dependency of single-particle crushing patterns on discretization using peridynamics. Powder Technol. **366**, 689–700 (2020)
31. Zhang, H., Qiao, P.Z.: A two-dimensional ordinary state-based peridynamic model for elastic and fracture analysis. Eng. Fract. Mech. **232**, 107040 (2020)
32. Madenci, E., Oterkus, E.: Peridynamic Theory and Its Applications, New York, America (2014)
33. Silling, S.A., Epton, M., Weckner, O., et al.: Peridynamic States and Constitutive Modeling. J. Elast. **88**, 151–184 (2007)
34. Breitzman, T., Dayal, K.: Bond-level deformation gradients and energy averaging in peridynamics. J. Mech. Phys. Solids. **110**, 192–204 (2018)
35. Madenci, E., Dorduncu, M., Phan, N., et al.: Weak form of bond-associated non-ordinary state-based peridynamics free of zero energy modes with uniform or non-uniform discretization. Eng. Fract. Mech. **218**, 106613 (2019)
36. Behzadinasab, M., Foster, J.T.: A semi-Lagrangian constitutive correspondence framework for peridynamics. J. Mech. Phys. Solids. **137**, 103862 (2020)
37. Chen, H.: Bond-associated deformation gradients for peridynamic correspondence model. Mech. Res. Commun. **90**, 34–41 (2018)
38. Behzadinasab, M., Foster, J.T.: Revisiting the third Sandia Fracture Challenge: a bond-associated, semi-Lagrangian peridynamic approach to modeling large deformation and ductile fracture. Int. J. Fract. **224**, 261–267 (2020)
39. Bazilevs, Y., Behzadinasab, M., Foster, J.T.: Simulating concrete failure using the Microplane (M7) constitutive model in correspondence-based peridynamics: Validation for classical fracture tests and extension to discrete fracture. J. Mech. Phys. Solids. **166**, (2022)
40. Yang, S.Y., Gu, X., Zhang, Q., et al.: Bond-associated non-ordinary state-based peridynamic model for multiple spalling simulation of concrete. Acta Mech. Sinica **37**, 1104–1135 (2021)
41. Shende, S., Behzadinasab, M., Moutsanidis, G., et al.: Simulating air blast on concrete structures using the volumetric penalty coupling of isogeometric analysis and peridynamics. Math. Models Methods Appl. Sci. **32**, 2477–2496 (2022)
42. Gu, X., Zhang, Q., Huang, D., et al.: Wave dispersion analysis and simulation method for concrete SHPB test in peridynamics. Eng. Fract. Mech. **160**, 124–137 (2016)
43. Ai, D.H., Zhao, Y.C., Wang, Q.F., et al.: Experimental and numerical investigation of crack propagation and dynamic properties of rock in SHPB indirect tension test. Int. J. Impact Eng. **126**, 135–146 (2019)
44. Ai, D.H., Zhao, Y.C., Wang, Q.F., et al.: Crack propagation and dynamic properties of coal under SHPB impact loading: Experimental investigation and numerical simulation. Theor. Appl. Fract. Mec. **105**, 102393 (2020)
45. Zhang, Y.N., Deng, H.W., Ke, B., et al.: Research on the Explosion Effects and Fracturing Mechanism of Liquid Carbon Dioxide Blasting. Mining Metall. Explor. **39**, 521–530 (2022)
46. Ha, Y.D., Lee, J., Hong, J.W.: Fracturing patterns of rock-like materials in compression captured with peridynamics. Eng. Fract. Mech. **144**, 176–193 (2015)
47. Lee, J., Ha, Y.D., Hong, J.W.: Crack coalescence morphology in rock-like material under compression. Int. J. Fracture. **203**, 211–236 (2016)
48. Wang, Y.T., Zhou, X.P., Xu, X.: Numerical simulation of propagation and coalescence of flaws in rock materials under compressive loads using the extended non-ordinary state-based peridynamics. Eng. Fract. Mech. **163**, 248–273 (2016)
49. Wang, Y.T., Zhou, X.P., Shou, Y.D.: The modeling of crack propagation and coalescence in rocks under uniaxial compression using

the novel conjugated bond-based peridynamics. Int. J. Mech. Sci. **128-129**, 614–643 (2017)
50. Zhou, X.P., Gu, X.B., Wang, Y.T.: Numerical simulations of propagation, bifurcation and coalescence of cracks in rocks. Int. J. Rock. Mech. Min. **80**, 241–254 (2015)
51. Zhou, X.P., Wang, Y.T.: Numerical simulation of crack propagation and coalescence in pre-cracked rock-like Brazilian disks using the non-ordinary state-based peridynamics. Int. J. Rock Mech. Min. **89**, 235–249 (2016)
52. Zhang, Y.B., Huang, D., Cai, Z., et al.: An extended ordinary state-based peridynamic approach for modelling hydraulic fracturing. Eng. Fract. Mech. **234**, 107086 (2020)
53. Wang, J.F., Qian, S.R.: Spallation Analysis of Concrete Under Pulse Load Based on Peridynamic Theory. Wireless Pers. Commun. **112**, 949–966 (2020)
54. Zhou, Z.Q., Li, Z.H., Gao, C.L., et al.: Peridynamic micro-elasto-plastic constitutive model and its application in the failure analysis of rock masses. Comput. Geotech. **132**, 104037 (2021)
55. Zhou, L.M., Zhu, S., Zhu, Z.D., et al.: Improved peridynamic model and its application to crack propagation in rocks. Roy. Soc Open. Sci. **9**, 221013 (2022)
56. Fei, M.P., Chen, L.S., Ying, Z.H., et al.: Simulations of crack propagation in rock-like materials using modified peridynamic method. Rock Soil Mech. **40**, 4112–4119 (2019) in Chinese
57. Yang, S.Q., Yang, Z., Zhang, P.C., et al.: Experiment and peridynamic simulation on cracking behavior of red sandstone containing a single non-straight fissure under uniaxial compression. Theor. Appl. Fract. Mec. **108**, 102637 (2020)
58. Silling, S.A., Askari, E.: A meshfree method based on the peridynamic model of solid mechanics. Comput. Struct. **83**, 1526–1535 (2005)
59. Gerstle, W., Sau, N., Silling, S.: Peridynamic modeling of concrete structures. Nucl. Eng. Des. **237**, 1250–1258 (2007)
60. Gerstle W.H., Sau, N., Sakhavand, N.: On peridynamic computational simulation of concrete structures. Spec. Publ. **265**, 245–264 (2009)
61. Li, S., Lu, H., Jin, Y., et al.: An improved unibond dual-parameter peridynamic model for fracture analysis of quasi-brittle materials. Int. J. Mech. Sci. **204**, 106571 (2021)
62. Li, S., Lu, H., Huang, X., et al.: Improved peridynamics approach for the progressive fracture of marine concrete. Ocean Eng. **255**, 111404 (2022)
63. Kilic, B., Madenci, E.: An adaptive dynamic relaxation method for quasi-static simulations using the peridynamic theory. Theor. Appl. Fract. Mech. **53**, 194–204 (2010)
64. Oakley, D.R., Knight, Jr. N.F.: Adaptive dynamic relaxation algorithm for non-linear hyperelastic structures Part I. Formulation. Comput. Methods Appl. Mech. Engng. **126**, 67–89 (1995)
65. Yang, Y.F., Tang, C.A., Xia, K.W.: Study on crack curving and branching mechanism in quasi-brittle materials under dynamic biaxial loading. Int. J. Fract. **177**, 53–72 (2012)
66. Hawong, J.S., Kobayashi, A.S., Dadkhah, M.S., et al.: Dynamic crack curving and branching under biaxial loading. Exp. Mech. **27**, 146–153 (1987)
67. Ha, Y.D., Bobaru, F.: Studies of dynamic crack propagation and crack branching with peridynamics. Int. J. Fracture. 162, 229–244 (2010)
68. Gong, F.Q., Yan, J.Y., Luo, S., et al.: Investigation on the Linear Energy Storage and Dissipation Laws of Rock Materials Under Uniaxial Compression. Rock Mech. Rock. Eng. **52**, 4237–4255 (2019)